Noname manuscript No.
(will be inserted by the editor)

Stable Boundary Layers with Subsidence: Scaling and Similarity of the Truly Steady State

Thijs Bon · Raúl Bayoán Cal · Johan Meyers

arXiv:2406.01751v1 [physics.flu-dyn] 3 Jun 2024

Received: DD Month YEAR / Accepted: DD Month YEAR

Abstract
The stable boundary layer (SBL) subjected to large-scale subsidence is studied through large-eddy simulations (LESs) with fixed surface temperature and a linear subsidence velocity profile. These boundary layers reach a truly steady state, where thermal equilibrium is established by a balance between surface cooling and subsidence-induced heating. We identify three governing dimensionless groups by scaling the governing equations with the geostrophic wind and Coriolis frequency, and systematically investigate the impact of these external parameters on global flow properties and mean profiles in the steady state. The SBL depth, low-level jet, and the magnitude of the turbulent momentum flux are reduced when the subsidence rate or Buoyancy number increases, while surface heat flux is enhanced. The shape of normalized mean profiles of temperature and heat flux is mainly determined by the subsidence rate, while they collapse for varying buoyancy and surface Rossby numbers. We develop empirical correlations for the stability parameter h_θ/L_O and a thermal shape factor, and propose a new unidirectional geostrophic drag law, to form a closed set of equations that estimates relevant flow properties from external parameters. The estimation errors compared to the LES data are less than 5% for friction velocity and surface heat flux, and at most 10% for the SBL depth h_θ. Within the surface layer, dimensionless velocity and temperature gradients in the steady SBL with subsidence show acceptable agreement to Monin–Obukhov similarity theory, while the collapse is improved when a recently proposed mixed scaling parameter, that includes h_θ/L_O, is used.

1 Introduction

One of the key challenges in atmospheric and environmental sciences is understanding of the stable boundary layer (SBL), which is relevant to the renewable energy sector, air quality and pollutant dispersion, numerical weather prediction and climate modelling (e.g. Steeneveld (2014), McWilliams et al. (2023), and references therein). The atmospheric boundary layer (ABL) commonly exhibits stable stratification during nighttime over land (also referred to as the nocturnal boundary layer or NBL), due to radiative cooling of the surface. SBLs can further be generated by advection of warm air over a colder surface, for example in maritime areas or in the polar regions. The main processes that govern the structure of the SBL are radiation, turbulence, horizontal advection and subsidence (Stull 1988; Wyngaard 2010).

T. Bon
Department of Mechanical Engineering, KU Leuven, Celestijnenlaan 300A-Bus 2421, B3001 Leuven
E-mail: thijs.bon@kuleuven.be

R. B. Cal
Portland State University, Department of Mechanical and Materials Engineering, Portland, Oregon 97207, USA

J. Meyers
Department of Mechanical Engineering, KU Leuven, Celestijnenlaan 300A-Bus 2421, B3001 Leuven

Subsidence, large-scale downward movement of air, and as a consequence near-surface flow divergence, is often associated with synoptic high-pressure systems, fair weather conditions and clear skies (Carlson and Stull 1985). Furthermore, polar areas experience persistent subsidence due to planetary-scale circulations (Holton 2004). Motivated by the relatively small magnitude of these vertical motions compared to horizontal velocity components and the difficulty to accurately measure them, subsidence is often neglected in numerical investigations of the SBL (Mirocha and Kosović 2010; Stoll et al. 2020). However, early observational studies already concluded that the heating rate associated with subsidence can be as large as the cooling rates due to turbulence and radiation (Carlson and Stull 1985; Mirocha et al. 2005), and should therefore not be neglected. In the present study, we investigate the SBL under influence of subsidence and the related steady state regime through an extensive set of large-eddy simulations (LESs). Although effects of subsidence on the SBL have been investigated previously, a systematic analysis of the full parameter space that plays a role in the SBL with subsidence has not been performed before.

In a stably stratified environment, subsidence brings down warm air from aloft, thereby reducing the boundary-layer height and affecting the atmospheric heat balance (Stull 1988). This can affect many other physical processes, such as dispersion of pollutants (Shi et al. 2022), and growth/ablation of a snow/ice pack due to changes in surface heat flux (Mirocha and Kosović 2010). Moreover, the formation of marine boundary layer clouds, which poses a significant source of uncertainty in climate models, is influenced by subsidence (Bellon and Stevens 2012; Chung et al. 2012). Prior work has demonstrated that incorporating atmospheric subsidence into numerical simulations improves the agreement with measurement data of the SBL over the Arctic Ocean (Mirocha and Kosović 2010) and the Antarctic Plateau (Vignon et al. 2017b; van der Linden et al. 2019). Other studies highlight the importance of including subsidence in modelling of the unstable boundary layer over both land (Blay-Carreras et al. 2014; Rey-Sanchez et al. 2021) and sea (Mazzitelli et al. 2014).

The LES study of Mirocha and Kosović (2010), which was based on observations from the Surface Heat Budget of the Arctic Ocean field experiment (SHEBA), showed that the addition of subsidence reduces vertical momentum fluxes while enhancing vertical heat flux, increases temperature gradients, and limits the growth of the boundary layer, leading to a "nearly steady boundary layer behaviour during periods of constant forcing". More recently, L19 performed centimetre-scale LESs of a weakly and very stable boundary layer and compared results to observational data from the Dome C station on the Antarctic Plateau, where the absence of the diurnal cycle during the Antarctic winter facilitated the examination of a long-lived SBL. They concluded that the inclusion of subsidence can result in a truly steady SBL, where the turbulent cooling towards the surface is balanced by the heating due to subsidence. This statistically steady state, characterized by a thermal equilibrium (see section 2.1), is the main focus in the present study. We note that the term "equilibrium" here should not be confused with equilibrium in developing turbulent boundary layers, which describes a situation where the normalized flow properties do not longer depend on streamwise position (Devenport and Lowe 2022).

In typical investigations of the SBL through LES or direct numerical simulation (DNS), a true steady state is never reached. Many of these studies are based on the well-documented case setup of the Global Energy and Water Cycle Experiment Atmospheric Boundary Layer Study 1 (GABLS1, Beare et al. (2006)), which currently is still used as a reference case to e.g., validate new LES codes (Van Heerwaarden et al. 2017), evaluate new subgrid models or surface parametrizations (Matheou and Chung 2014; Maronga et al. 2020; Dai et al. 2021) and assess grid-size sensitivity of LES models (Maronga and Li 2022). Slightly modified configurations have been used to study effects of increasing stability (Huang and Bou-Zeid 2013; Sullivan et al. 2016; Narasimhan et al. 2023), heterogeneous surface temperatures (Stoll and Porté-Agel 2009; Mironov and Sullivan 2016), or interactions between the SBL and wind farms (Allaerts and Meyers 2018; Strickland et al. 2022). The GABLS1 setup is characterized by a constant cooling rate as the lower boundary condition, meaning that the surface temperature keeps decreasing in time. In studies that employ DNS to study the SBL, there is more variety in the surface temperature boundary condition, involving either a prescribed surface heat flux (e.g. Nieuwstadt 2005; Flores and Riley 2011; Gohari and Sarkar 2017), fixed bottom temperature (Ansorge and Mellado 2014; Shah and Bou-Zeid 2014), or a combination thereof (Gohari and Sarkar 2018). Because the surface cooling is not compensated by any heat source, none of the simulations in the aforementioned studies reaches a truly steady state, where both the turbulent and thermal energy of the

system are in (statistical) equilibrium. The "quasi-steady" state that the SBL reaches after a finite time is commonly employed, in which the mean profiles of velocity and turbulence statistics remain constant while only the temperature profile keeps changing. This quasi-steady period is then used to analyze results and compare cases, while the domain-averaged temperature still declines (see Eq. (1)). In numerous applications however, it is desired to have long averaging times under truly stationary conditions, without any transient effects, to permit more systematic analysis and comparison of multiple different simulations. For example, the study of large-scale secondary motions that can be induced by heterogeneous surface roughness or temperatures, requires long averaging times (Bon and Meyers 2022; Castro et al. 2021; Schäfer et al. 2022). When employing LES for a systematic analysis of the effects of large wind farms on atmospheric heat fluxes, examination of stationary statistics considerably simplifies understanding (Sescu and Meneveau 2014; Maas and Raasch 2022). Moreover, in assessments of the sensitivity of an LES code to the grid spacing or the subgrid-scale model, constantly decreasing surface temperature in typical SBL simulations prevents using long averaging times (Maronga and Li 2022).

In the next section (2.1) , we start with a brief description of thermal equilibrium in the SBL with subsidence. The LES code and numerical methodology are subsequently outlined in Sect. 2.2. Based on dimensional analysis, we identify the relevant non-dimensional groups in Sect. 2.3, and perform a series of LESs where the surface temperature, subsidence rate and surface roughness are varied. The case setup can be roughly viewed as a combination of the GABLS1 case and the configuration used by L19, as further detailed in Sect. 2.4. Based on the LES results, we examine how the steady state depends on the relevant external parameters in Sect. 3. Different methods of estimating the SBL depth are compared in Sect. 3.2, followed by an investigation of scaled mean profiles (Sect. 3.3). In Sect. 3.4, a geostrophic drag law is proposed for the steady SBL with subsidence, and present model equations that accurately estimate global flow properties of interest based on external parameters. An assessment of the validity of the widely used Monin–Obukhov similarity theory (MOST) in the presence of subsidence is given in Sect. 3.5. Finally, the main conclusions are summarized in Sect. 4.

2 Theory and Methods

2.1 Conditions for Thermal Equilibrium

In typical idealized LES, subsidence and radiation effects are not taken into account, such that the temporal evolution of the potential temperature θ is determined by the divergence of the turbulent heat flux $\partial q/\partial x_i$ (see also Eq. (8) further below). Taking the horizontal average and integrating vertically, we find:

$$\int_0^h \frac{\partial \langle\theta\rangle}{\partial t}\mathrm{d}z = -\int_0^h \frac{\partial \langle q_z\rangle}{\partial z}\mathrm{d}z = \langle q_z\rangle_0 \equiv q_0 < 0 \tag{1}$$

where z denotes the vertical coordinate, angular brackets denote horizontal averaging, $\langle q_z\rangle = \langle w'\theta'\rangle + \langle q_z^{sgs}\rangle$ is the total (turbulent + subgrid-scale) heat flux, h can be any height above which q_z is assumed to vanish (i.e. $\langle q_z\rangle_h = 0$), and q_0 is the surface heat flux. Note that the order of the integral and the derivative on the left-hand side can be changed provided that h remains constant. Since the surface heat flux in an SBL is per definition non-zero and negative, Eq. (1) shows that the mean temperature in the boundary layer will keep decreasing if there are no additional heat sources.

This changes when a subsidence term of the form $Q_s = -w_s(z)(\partial\langle\theta\rangle/\partial z)$ is added to the temperature equation, acting as a heat source. A number of different parametrizations for the subsidence velocity profile $w_s(z)$ have been proposed in previous studies, such as piecewise linear (van der Linden et al. 2019; Maas and Raasch 2022), cubic (Mirocha and Kosović 2010), polynomial (Mazzitelli et al. 2014) or exponential (Bellon and Stevens 2012) shapes. In order to minimize the number of external parameters, we adopt a simple linear subsidence profile $w_s(z) = -\Gamma_w z$ (with $\Gamma_w > 0$), similar to e.g. Chung et al. (2012). Note that due to continuity, the subsidence rate Γ_w directly corresponds to the magnitude of the associated large-scale horizontal divergence, which is thus assumed constant with height (Mazzitelli et al. 2014).

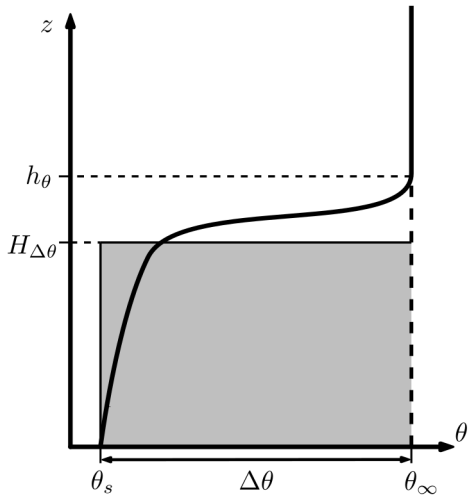

Fig. 1 Schematic diagram of SBL temperature profile with geometrical definitions of thermal boundary-layer depth h_θ, integral depth scale $H_{\Delta\theta}$ and global temperature difference $\Delta\theta$. The shaded area within the rectangle $H_{\Delta\theta}\Delta\theta$ equal the area under the potential temperature curve. Figure inspired by Fig. 12.4 in Stull (1988)

Including the subsidence term, the horizontally-averaged temperature equation for the steady state can be written as:

$$\frac{\partial\langle\theta\rangle}{\partial t} = 0 = -\frac{\partial\langle q_z\rangle}{\partial z} + \Gamma_w z\frac{\partial\langle\theta\rangle}{\partial z}, \tag{2}$$

showing that the flow is in thermal equilibrium if cooling by vertical heat-flux divergence is equal to heating by subsidence (L19). An important implication of Eq. (2) is that thermal equilibrium can only be achieved if the non-turbulent free atmosphere or residual layer is unstratified, because the turbulent heat flux $q_z = 0$ there.

Performing the same integration as in Eq. (1) then leads to:

$$q_0 = -\Gamma_w \int_0^h z\frac{\partial\langle\theta\rangle}{\partial z}\mathrm{d}z = -\Gamma_w \left(z\langle\theta\rangle|_0^h - \int_0^h \langle\theta\rangle \mathrm{d}z \right) \tag{3}$$

where the last equality follows from partial integration. As usual in LES of the SBL, we only consider dry air under the Boussinesq-approximation, allowing us to change the reference temperature by a constant. Furthermore, following Fig. 1, it is assumed that $h = h_\theta$ is the thermal boundary-layer height above, where the temperature remains equal to the constant free-atmosphere temperature ($\theta(z \geq h_\theta) = \theta_\infty$) and the surface temperature $\theta_s = \theta_\infty - \Delta\theta$ is fixed, such that the substitution θ by a temperature deviation $\theta_\delta = \theta - \theta_\infty$ is made without loss of generality. Consequently, the first term on the right-hand side of Eq. (3) vanishes and obtain:

$$q_0 = \Gamma_w \int_0^{h_\theta} \langle\theta_\delta\rangle \mathrm{d}z = \Gamma_w \Delta\theta H_{\Delta\theta}. \tag{4}$$

The integral of the temperature deviation can be interpreted as the 'accumulated cooling', and is alternatively written as $\Delta\theta H_{\Delta\theta}$, where $H_{\Delta\theta} = 1/\Delta\theta \int_0^{h_\theta} \langle\theta_\delta\rangle \mathrm{d}z$ is the integral depth scale of the SBL (see Fig. 1 and p. 504 in Stull (1988)). It is noted that, in the community that studies developing thermal boundary layers, $H_{\Delta\theta}$ is referred to as the thermal displacement thickness (Wang and Castillo 2003).

Equation (4) shows that the SBL in our simplified framework reaches a steady state when the surface heat flux (left-hand side) is equal to the bulk heat flux due to subsidence heating (right-hand side), calculated as the integrated temperature deviation multiplied by the linear subsidence rate (Stull 1988, p. 515). Moreover, Eq. (2) shows that there is an explicit relation between mean profiles of temperature and turbulent heat flux. However, as pointed out by L19, the internal distribution of heat flux and temperature in the boundary layer, and likewise the surface heat flux, (thermal) boundary-layer height and mean temperature, remain unknown a priori. The set of

simulations that we perform aims to shed light on relations between these parameters and assess similarity of mean profiles, as discussed in Sect. 3.3.

Heuristically, one can assume that the integral $\int_0^{h_\theta} \langle\theta_\delta\rangle \mathrm{d}z$ is proportional to $h_\theta \Delta\theta$, with a proportionality parameter S_θ that depends on the shape of the temperature profile. This "shape factor" is then defined as:

$$S_\theta = \frac{1}{h_\theta \Delta\theta} \int_0^{h_\theta} \langle\theta_\delta\rangle \mathrm{d}z = \frac{H_{\Delta\theta}}{h_\theta} = \frac{q_0}{\Gamma_w h_\theta \Delta\theta} \tag{5}$$

where the last equality only holds in thermal equilibrium and follows from Eq. (4). Note that this same parameter also appears in Eq. (2) if q_z, θ and z are scaled with $q_0, \Delta\theta$ and h_θ. The denominator $(\Gamma_w h_\theta \Delta\theta)$ could be interpreted as the maximal possible bulk heat flux due to subsidence, that would occur if all subsidence heating would take place at an infinitely thin temperature inversion layer of strength $\Delta\theta$ at height h_θ. Hence, S_θ can also be explained as the ratio of the actual bulk subsidence heat flux (see Eq. (4)) and the theoretical maximum, or the 'efficiency' of the subsidence heating. Evidently, $S_\theta = 1/2$ in case of a linear temperature profile between $z = 0$ and $z = h_\theta$, while in general S_θ should be between 0 and 1 (see also Fig. 1 here and Fig. 12.5 in Stull (1988)). In Sect. 3.3 we will investigate how S_θ is affected by external simulation parameters.

2.2 Numerical Methodology

The governing equations of our LES model are filtered versions of the continuity, Navier-Stokes and potential-temperature equations for incompressible flow under the Boussinesq approximation:

$$\frac{\partial u_i}{\partial x_i} = 0, \tag{6}$$

$$\frac{\partial u_i}{\partial t} = -\frac{\partial}{\partial x_j}(u_i u_j + \tau_{ij}^{sgs}) - \frac{\partial p^\star}{\partial x_i} + f_c \epsilon_{ij3}(u_j - G\delta_{j1}) + \frac{g}{\theta_r}(\theta_\delta - \langle\theta_\delta\rangle)\delta_{i3}, \tag{7}$$

$$\frac{\partial \theta_\delta}{\partial t} = -\frac{\partial}{\partial x_j}(u_j \theta_\delta + q_j^{sgs}) + \Gamma_w x_3 \frac{\partial \langle\theta_\delta\rangle}{\partial x_3}, \tag{8}$$

where indices $i = 1, 2, 3$ correspond to respective horizontal (x, y) and vertical (z) directions, u_i are the filtered velocity components and $\theta_\delta = \theta - \theta_\infty$ is the filtered temperature deviation from the top temperature. The boundary layer is subjected to a large-scale pressure forcing, determined by the Coriolis frequency $f_c = 1.39 \times 10^{-4}\ \mathrm{s}^{-1}$ and the geostrophic wind speed $G = 8\ \mathrm{m\ s}^{-1}$. The gravitational acceleration $g = 9.81\ \mathrm{m/s}^2$, and the reference temperature $\theta_r = \theta_\infty = 263.5\ \mathrm{K}$. These values are equal across all simulations and align with those in the GABLS1 case (Beare et al. 2006)). As described in the previous section, Γ_w is the subsidence rate, i.e. the gradient of the subsidence velocity profile in s^{-1}. Following L19, we use the horizontally averaged vertical temperature gradient rather than the local one, and neglect horizontal velocity divergence in the momentum equation (see Appendix 1 in their work for justification). The subgrid-scale (SGS) fluxes τ_{ij}^{sgs} and q_j^{sgs} are modelled with the turbulent kinetic energy (TKE) model, based on Deardorff (1980), which may be the most widely used SGS model in LES (Gibbs and Fedorovich 2016; Stoll et al. 2020). The modified filtered pressure $p^\star$ is in fact the deviation from the background pressure, divided by a reference density, and includes the trace of the subgrid stress tensor (Allaerts and Meyers 2015).

The governing equations (6)-(8) are solved using the SP-Wind solver, an in-house DNS/LES code developed over the past 15 years at KU Leuven. It has been widely used to study the interaction between wind-farms and the (stably) stratified Ekman layer (Goit and Meyers 2015; Allaerts 2016; Allaerts and Meyers 2018; Lanzilao and Meyers 2024), as well as stably stratified flows over thermally inhomogeneous surfaces (Bon et al. 2023). In SP-Wind, time integration is performed using a classical fourth-order Runge–Kutta scheme with a fixed Courant–Friedrichs–Lewy (CFL) number of 0.4. The code employs pseudo-spectral discretization in the horizontal directions with the 3/2-dealiasing rule for the nonlinear terms, and a fourth-order energy conserving finite-difference scheme for the vertical direction (Verstappen and Veldman 2003). Consequently, the horizontal boundary conditions are periodic, while at the top of the domain symmetry

conditions for horizontal velocity components and potential temperature ($(\partial(u,v,\theta)/\partial z = 0)$ are applied, and the vertical velocity (w) is 0.

At the lower boundary of the domain, we apply MOST to model the surface fluxes for momentum and temperature. A note on using MOST as a boundary condition is presented in Appendix 3. The surface flux parametrization in MOST depends on the roughness lengths for momentum (z_{0m}) and heat (z_{0h}), and the fixed surface temperature $\theta_s = \theta_\infty - \Delta\theta$. In order to limit our parameter space, we take $z_{0h} = z_{0m} = z_0$. For further details on the SP-wind code, implementation of MOST and the TKE subgrid model, we refer to Allaerts (2016) and Allaerts and Meyers (2018). The latest version of SP-Wind employs a full 3-dimensional domain decomposition for efficient parallel computation, allowing to run the majority of simulations on 12 nodes, each containing 128 AMD Epyc 7763 cores in the HPC cluster of the Flemish Supercomputing Center (VSC).

2.3 Dimensional Analysis

In the idealized LES of stably stratified boundary layers with subsidence considered, there are at least five relevant external parameters. Provided that the top of the computational domain is high above the turbulent boundary layer and the surface temperature is fixed, both the top temperature θ_∞ and the surface temperature θ_s remain constant. Therefore, the global buoyancy difference $(g/\theta_r)(\theta_t - \theta_s) = (g/\theta_r)\Delta\theta \equiv \Delta B$ is one input to our simulations. With that, the full set of governing parameters is $\{G, f_c, z_0, \Delta B, \Gamma_w\}$. Applying the Buckingham-Pi theorem to these five parameters which involve only two dimensions (length and time), three non-dimensional Π-groups are formed:

$$Ro_0 = \frac{G}{f_c z_0}, \quad Bu = \frac{\Delta B}{G f_c}, \quad \text{and} \quad \Pi_w = \frac{\Gamma_w}{f_c}. \tag{9}$$

The first group is a Rossby number based on the surface roughness length z_0 and geostrophic wind G, commonly referred to as the surface Rossby number (e.g. Tennekes 1973; Zilitinkevich and Esau 2002). The second is the Buoyancy number Bu, a global stability parameter that characterizes thermal stratification across an Ekman layer (Csanady 1974; Swinbank 1974). It is a ratio between buoyancy forces and Coriolis forces, or can be viewed alternatively as a product of a Richardson number $Ri = \Delta B h / G^2$ and a Rossby number $Ro_h = G/(fh)$, where h would be the boundary-layer height. The last group, Π_w, determines the magnitude of the subsidence and can be interpreted as the ratio between the timescales of subsidence heating and Coriolis force. Note that this is a purely practical choice of scaling the subsidence with one of the external parameters, since f_c and Γ_w do not appear in the same equation (see Eqs. (6)-(8))

2.4 Suite of Simulations

Based on the dimensionless groups in Eq. (9), three sets of simulations are performed where one of the parameters is changed while the others are kept at a reference value. As mentioned above, G, f_c and g/θ_r are held constant over all simulations, thus only z_0, $\Delta\theta$ and Γ_w are varied. These three simulation sets are referred with letters 'Z', 'T' and 'S', respectively. The simulation with the 'default' values $z_0 = 10^{-3}$ m ($Ro_0 = 5.8 \times 10^7$), $\Delta\theta = 3$ K ($Bu = 100$) and $\Gamma_w = 1.25 \times 10^{-5}$ s^{-1} ($\Pi_w = 0.09$) is referred to as 'S3T2Z2'. An overview of all simulations is provided in Table 1.

In set 'Z', the surface roughness is varied between 10^{-4} m, as typically used to represent sea surface (Liu et al. 2021a; Lanzilao and Meyers 2024) and 10^{-1} m which was used in the GABLS1 case to represent onshore conditions (Beare et al. 2006). The reference value of 10^{-3} m lies in between, and corresponds to that used by L19 to represent the Dome C site in Antarctica. In recent LES studies of SBLs (van der Linden et al. 2019; Couvreux et al. 2020; Narasimhan et al. 2023), the roughness length for heat is one order of magnitude smaller than for momentum, as also recommended by Vignon et al. (2017a) based on measurements in polar regions. However, Couvreux et al. (2020) report little sensitivity of simulation results to changing z_{0h} from 10^{-4} m to 10^{-3} m, and confirmed through preliminary simulations.

The range of temperature differences in set 'T' spans from $\Delta\theta = 1.5$ K to 12 K. The 'base' temperature difference of 3 K roughly corresponds to the difference between the temperature at

the surface and the top of the inversion layer in the GABLS1 case, allowing direct comparison of mean profiles to the present simulations (see Fig. 2k-o)

In set 'S', the subsidence rate Γ_w is varied over two orders of magnitude, from 2.5×10^{-6} s^{-1} to 2×10^{-4} s^{-1}, while the cases in the other sets have the base value of 1.25×10^{-5} s^{-1}. To put these values into context, Carlson and Stull (1985) estimated horizontal divergence rates of $0.09 - 3.3 \times 10^{-5}$ s^{-1} based on a field experiment in Oklahoma. The majority of aforementioned LES studies that include subsidence, assumed a subsidence rate or horizontal divergence in the order of $10^{-6} - 10^{-5}$ s^{-1}. In particular, L19 essentially employs a linear subsidence velocity profile with gradient 4×10^{-5} s^{-1} up to 100 m above the surface, inferred from ERA-Interim model reanalysis and simulations from Baas et al. (2019).

2.4.1 Initialization and Time Development

All simulations are initialized with a uniform velocity $u = G$ in the $x-$direction, with random perturbation of $0.1G$ added to the velocity components below $h_p = 100$ m to trigger turbulence. The initial temperature profile increases linearly from θ_s to $\theta_\infty = \theta_s + \Delta\theta$ at $h_i = 200$ m and is equal to θ_∞ above. In preliminary simulations, initial conditions were varied by e.g. changing the initial inversion height h_i or starting from a constant temperature θ_∞ and gradually cooling the surface temperature towards the final value θ_s (similar to the DNSs of Gohari and Sarkar (2018) or LESs of L19 and Maronga et al. (2020)). Crucially, the initial conditions did not have an effect on the mean profiles in the final equilibrium state, except the time needed to reach this steady state. Furthermore, in the latter scenario, a notably stronger inertial oscillation in the upper part of the domain was observed. This can be attributed to turbulent perturbations penetrating deeply into the neutral free atmosphere, leading to differences between the horizontal velocity components and geostrophic wind, consequently triggering the inertial oscillation (Blackadar 1957; van de Wiel et al. 2010). By applying a temperature gradient up to a sufficient height from the onset of the simulations, there is a stably stratified layer above the initial turbulent perturbations, that prevents turbulence to enter into the neutral free atmosphere.

In all simulations, the amplitude of the inertial oscillation, quantified by considering the time development of $\langle u \rangle$ and $\langle v \rangle$ averaged over the upper 25% of the domain, was smaller than 1% of the geostrophic wind G. Therefore, we were not required to use forced damping methods in the upper part of the domain, such as the geostrophic damping approach proposed by Stipa et al. (2023) or the widely used Rayleigh Damping Layer (Klemp and Lily 1977; Lanzilao and Meyers 2022). The latter is commonly applied in numerical simulations to prevent spurious reflection of gravity waves at the upper boundary, but unnecessary here due to the unstratified free atmosphere.

To assess whether a simulation has reached thermal equilibrium, the instantaneous sum of the surface heat flux and the domain-integrated subsidence heating are diagnosed as:

$$Q_{\mathrm{sum}}(t) = q_0(t) + \int_0^{L_z} \Gamma_w z \frac{\partial \langle \theta \rangle}{\partial z}(t) \mathrm{d}z, \tag{10}$$

which should be close to 0 in the steady state. The total simulation time for each case is reported in Table 1, and all statistics are collected over the last $T_{av} = 2\pi / f_c \approx 12.56$ hours, corresponding to one inertial period. The ratio $R_q = Q_{\mathrm{sum}}/q_0$, averaged over T_{av}, was ensured to be smaller than 1%, as reported in Table 1. In the remainder of the text, all variables can be assumed to be time-averaged and in the statistically steady state.

2.4.2 Resolution and Domain Size

All simulations are performed on a domain of $L_x \times L_y \times L_z = 400^3$ m, equal to the GABLS1 configuration. The maximum boundary-layer depth h of approximately 200 m in our cases is also comparable, although it is smaller in most cases (see next section and Table 1). To assess the sensitivity to domain size, two simulations of case S3T2Z2 were run, where the respective horizontal and vertical dimensions were doubled, which had negligible effect on mean profiles of first and second order statistics. The only observable difference was in the peak of the turbulent temperature fluctuation $\langle \theta'^2 \rangle$ that occurs at the height of the inversion layer (not shown), for the case where the horizontal domain size was doubled. This peak in temperature variance is assumed

Table 1 Overview of simulations and bulk quantities. The external parameters are subsidence rate Γ_w, global temperature difference $\Delta\theta$, surface roughness z_0, and the corresponding dimensionless subsidence, buoyancy and surface Rossby numbers (Π_w, Bu, Ro_0 as defined in (9)). Internal parameters are friction velocity u_*, kinematic surface heat flux q_0, thermal boundary-layer height h_θ, Obukhov length L_O. The total runtime t_r of each simulation is reported in the last column. Note that the last two rows are simulations by L19, derived from their Table 2

Case	Γ_w (s^{-1})	$\Delta\theta$ (K)	z_0 (m)	Π_w	Bu	Ro_0	u_* (m s^{-1})	q_0 (K m s^{-1})	h_θ (m)	L_O (m)	t_r (h)	R_q (%)
S1	2.5×10^{-6}	3	10^{-3}	0.02	100	5.8×10^{7}	0.232	-1.31×10^{-3}	190	644	84	0.05
S2	6.25×10^{-6}	3	10^{-3}	0.04	100	5.8×10^{7}	0.223	-2.28×10^{-3}	152	327	60	0.66
S3T2Z2	1.25×10^{-5}	3	10^{-3}	0.09	100	5.8×10^{7}	0.212	-3.39×10^{-3}	134	188	60	0.04
S4	2.5×10^{-5}	3	10^{-3}	0.18	100	5.8×10^{7}	0.198	-4.83×10^{-3}	120	108	36	0.58
S5	5.0×10^{-5}	3	10^{-3}	0.36	100	5.8×10^{7}	0.183	-6.42×10^{-3}	109	63.3	36	0.08
S6	1.0×10^{-4}	3	10^{-3}	0.72	100	5.8×10^{7}	0.168	-8.23×10^{-3}	96.1	38.6	24	0.74
S7	2.0×10^{-4}	3	10^{-3}	1.44	100	5.8×10^{7}	0.159	-10.2×10^{-3}	82.0	26.3	24	-0.01
T1	1.25×10^{-5}	1.5	10^{-3}	0.09	50	5.8×10^{7}	0.222	-2.16×10^{-3}	176	341	48	-0.10
T3	1.25×10^{-5}	6	10^{-3}	0.09	201	5.8×10^{7}	0.196	-5.10×10^{-3}	101	98.5	60	0.83
T4	1.25×10^{-5}	12	10^{-3}	0.09	402	5.8×10^{7}	0.172	-7.23×10^{-3}	74.2	46.9	84	0.53
Z1	1.25×10^{-5}	3	10^{-4}	0.09	100	5.8×10^{8}	0.187	-2.85×10^{-3}	115	154	60	0.40
Z3	1.25×10^{-5}	3	10^{-1}	0.09	100	5.8×10^{5}	0.278	-5.02×10^{-3}	185	287	60	-0.41
GABLS1	0		10^{-1}	0	-	5.8×10^{8}	0.263	-10.9×10^{-3}	205	112	9	-
WSBL-B24	4.0×10^{-5}	25	10^{-3}	0.29	626	8.6×10^{7}	0.183	-25.6×10^{-3}	52.2	14.3	32	-0.31
WSBL-L19	4.0×10^{-5}	25	10^{-3}	0.29	626	8.6×10^{7}	0.184	-24.6×10^{-3}	51.9	15.6	30	-
VSBL-L19	4.0×10^{-5}	25	10^{-3}	0.29	2145	2.5×10^{7}	0.0356	-3.08×10^{-3}	5.93	0.915	23	-

to be related to internal waves in the very stable capping inversion (Saiki et al. 2000; Lloyd et al. 2022). As already argued by Beare et al. (2006), domain lengths of multiple kilometres would be required to catch the full extent of these gravity waves, which is beyond the interest of the present work.

Regarding resolution, a grid size of $128 \times 128 \times 256$ points is utilized, corresponding to a horizontal grid spacing of $\Delta_x = \Delta_y = 3.125$ m and $\Delta_z = 1.56$ m in the vertical direction. Allaerts (2016) is followed by using a finer resolution in the vertical direction than in the horizontal, as is common for codes with pseudo-spectral discretization in horizontal directions (e.g. Stoll and Porté-Agel 2009; Huang and Bou-Zeid 2013).

Because increasing stratification leads to a decrease in TKE, the dependency on the grid resolution and SGS model is amplified in simulations where the stability is stronger (Sullivan et al. 2016; van der Linden et al. 2019). Therefore, the grid sensitivity is evaluated for the three scenarios exhibiting the strongest stratification, as measured by stability parameter h_θ/L_O, with $L_O = \theta_r u_*^3 (\kappa g q_0)^{-1}$ the well-known Obukhov length (cases S6, S7 and T4, see Table 1). Details on this resolution study are provided in Appendix 1, where it is concluded that the mesh is sufficiently fine for the purpose of this study. Specifically, mean profiles are shown to be hardly affected by doubling of the grid resolution, and surface fluxes change less than 2.5%.

2.4.3 Two Reference Simulations

In addition to the simulations discussed above, two reference simulations are included which provide the ability to compare results to well-known cases from literature. First, the GABLS1 case was run, as was already used previously to validate the SP-Wind code for SBLs (see Allaerts (2016) for more details). Note that the same grid spacing was used here as in the other simulations. Secondly, to validate our code against a previous simulation that included subsidence, we ran the 'Weakly Stable Boundary Layer (WSBL)' case from L19. Both our GABLS1 and 'WSBL-B24' simulations are also included in Table 1. Additionally, the external parameters and bulk quantities from the WSBL and VSBL (Very Stable Boundary Layer) cases from L19 are reported in the last two rows. Of importance, cases from L19 employ a substantially larger global temperature difference of 25 K, while the subsidence rate lies in between our cases S4 and S5. The only difference between the WSBL and VSBL case is the geostrophic wind speed, which is reduced from 12 m/s to 3.5 m/s, thereby effectively increasing the Buoyancy number and lowering the surface Rossby number. More details on the WSBL-B24 and WSBL-L19 simulations, along with a comparison of mean profiles, is provided in Appendix 2. In general, the comparison yielded satisfactory results, especially when taking into account that the MicroHH code used by L19 employs a different discretization method and SGS model.

3 Results

3.1 Overview of Mean Profiles

The effect of each of the governing parameters in Eq. (9) is explored by discussing the horizontal- and time-averaged profiles of momentum, temperature and their respective fluxes for sets S, T and Z as displayed in Fig. 2. In all cases, the velocity magnitude $M = (\langle u \rangle^2 + \langle v \rangle^2)^{1/2}$ shows a supergeostrophic wind speed of about 9 m/s. This so-called low-level jet (LLJ) is often observed in both simulations and observations of the (stably) stratified atmosphere, and can have many possible causes (Stull 1988; Mahrt 1999). The formation of the LLJ in idealized LES of the SBL is often related to the inertial oscillation due to the Coriolis force. However, the LLJ in the present simulations is stationary. From the top row, it is evident that increasing subsidence rate decreases the height of the LLJ and the near-surface shear, whereas wind veer is increased. In addition, stronger subsidence reduces the turbulent vertical momentum flux $\tau_z = (\langle \tau_{xz} \rangle^2 + \langle \tau_{yz} \rangle^2)^{1/2}$ (with $\tau_{iz} = u_i' w' + \tau_{iz}^{sgs}$, i.e. the sum of resolved and subgrid shear stress) and increases the surface heat flux q_0. For low subsidence rates, there is a well-mixed layer with almost constant temperature capped by a strong inversion layer, resembling the widely studied 'Conventionally Neutral Boundary Layer' (CNBL) profile with zero free-atmosphere stratification (Liu et al. 2021b, and references therein). As subsidence rate increases, the height of this capping inversion decreases,

and eventually the temperature gradient becomes more or less constant throughout the boundary layer for the cases with strongest subsidence.

The second row of Fig. 2 shows the mean profiles for set T, where the temperature difference $\Delta\theta$ between the free-stream and the surface is varied (see panel i). Effects of increasing $\Delta\theta$ on the profiles of momentum are qualitatively similar to rising subsidence rate, i.e. the LLJ height descends, wind turns more sharply and surface stress decreases. Regarding the thermal profiles (panels i and j), the height of the inversion layer decreases while the surface heat flux increases.

The effect of surface roughness (or Rossby number) on mean profiles is presented in the bottom row of Fig. 2. It is evident that a rougher surface enhances turbulence generation and therefore increases vertical fluxes of momentum and heat, and the height of the LLJ. The temperature profiles seem unaltered in the lower part of the boundary layer, whereas only the height of the inversion layer increases with larger z_0. The grey dashed line in panels k-o, representing the GABLS1 case, displays roughly similar profiles to case C4, which has equal z_0. Note that for the temperature profile, $\theta_\infty = 266$ K is estimated to match the top of the inversion layer in the GABLS1 case with our simulations with subsidence (see also 5). The main deviation is in the vertical heat flux q_z, which is approximately linear in the GABLS1 case, in agreement with local scaling (Nieuwstadt 1984), while in our case the equilibrium equation (1) is satisfied (as further discussed in Sect. 3.3).

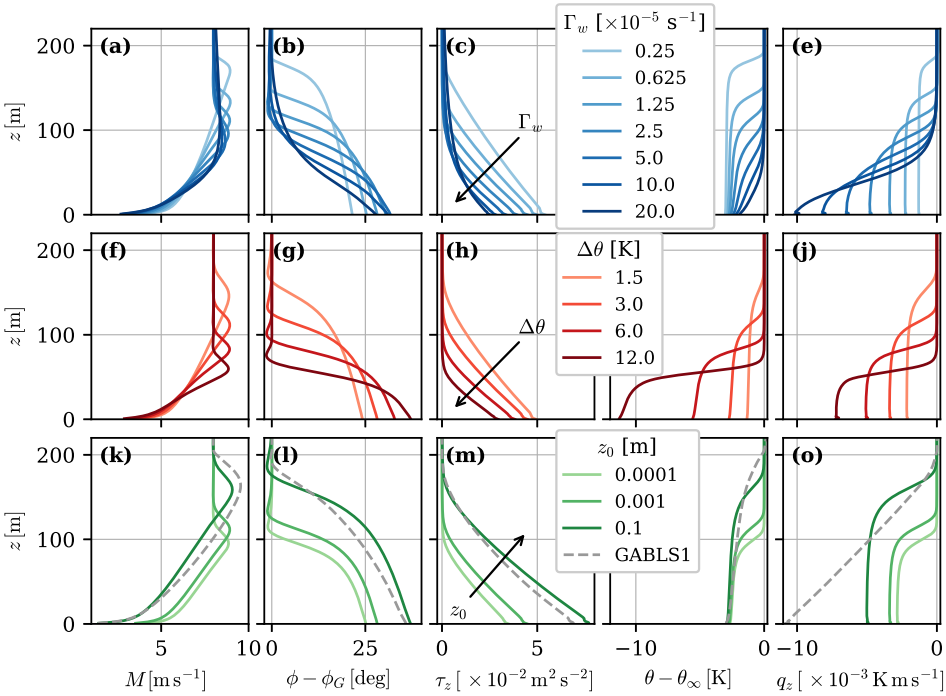

Fig. 2 Overview of mean profiles. Columns represent horizontal wind speed magnitude, flow angle, vertical momentum flux, potential temperature and heat flux. Rows represent simulation set S, where subsidence rate is varied (top), set T, where the temperature difference is varied (middle), and set Z, where the surface roughness is varied (bottom). Lines with darker colors indicate higher values of Γ_w, $\Delta\theta$ and z_0, respectively. See table 1 for a full description of the depicted simulations

3.2 Stable Boundary-Layer Depth

In order to scale the vertical coordinate of the mean profiles in Fig. 2, a length scale that characterizes the SBL depth is required. As the SBL often blends smoothly into the residual layer

above, accurately measuring its height is difficult, resulting in the existence of numerous estimation approaches (Stull 1988, see e.g. p. 503). To illustrate this, six methods, frequently used in LES studies, are enlisted to characterize the SBL depth (partly inspired by Chinita et al. (2022)):

1. h_τ: the height where the momentum flux vanishes, estimated as the height where τ_z is 5% of its surface value and then performing a linear extrapolation to the height where it would be 0, i.e. $h_\tau = z(\tau_z = 0.05u_*^2)/0.95$ (e.g. Beare et al. 2006; Huang and Bou-Zeid 2013; van der Linden et al. 2019).
2. $h'_\tau = z(\tau_z = 0.05u_*^2)/(1 - 0.05^{2/3}) \approx 1.1h_\tau$: similar to h_τ but with different extrapolation (Liu et al. 2021b), motivated by the expected power-law shape of the shear stress profile in an SBL as derived by Nieuwstadt (1984), i.e. $\tau_z/u_*^2 = (1 - z/h)^{3/2}$.
3. h''_τ: obtained by performing a least squares fit of the power-law profile $\tau_z/u_*^2 = (1 - z/h)^{3/2}$ to the shear-stress profiles in the LES (Narasimhan et al. 2023).
4. h_J: the position of the low-level jet (where velocity magnitude M is a maximum.)
5. $h_{\nabla\theta}$: the level where the temperature gradient is a maximum (Sullivan et al. 2016; McWilliams et al. 2023).
6. h_E: the height where the TKE reduces to 5% of the value at the first model level (Chinita et al. 2022).

In the present study however, the thermal boundary-layer height h_θ is used, because of its key role in the equations for thermal equilibrium (see Sect. 2.1). In practice, h_θ is approximated as the height where $(\langle\theta\rangle - \theta_s)/\Delta\theta = 99\%$. The six enlisted SBL depth estimations are compared to h_θ in Fig. 3. The figure shows h_i/h_θ for all cases. The choice of $\Pi_w^{1/2}$ on the horizontal emphasizes that the largest difference between all estimation methods occurs for the two cases with strongest subsidence. Ignoring these two cases, the estimates based on turbulent shear stress (in particular h'_τ and h''_τ) and TKE give similar results, and differ mostly less than 10% from h_θ (see zoom in panel b.). Further, the height of the LLJ is consistently about 80-90% of h_θ. The level where the maximal temperature gradient occurs relative to h_θ descends with increasing subsidence rate. This estimation method, proposed by Sullivan et al. (2016) to ensure the turbulent region above the LLJ is also included in the SBL depth, works well if there is a clear inversion layer with large gradients compared to the lower SBL, but fails in cases S6 and S7 since the maximum temperature gradient occurs very close to the surface. Regarding these two extreme cases, it is evident that estimates based on turbulent shear stress or TKE are much higher than the thermal boundary layer (see also Fig. 5 and related discussion).

The markers at $\Pi_w = 0$ in Fig. 3 represent the GABLS1 case. Here, the thermal boundary-layer height is estimated to be the level of maximum curvature in the temperature profile, i.e. where $|\partial^2\langle\theta\rangle/\partial z^2|$ has a maximum. This results in $h_\theta = 205$ m, which visually corresponds well to the transition from the inversion layer to the free atmosphere. Note that $\theta(z = h_\theta) \approx \theta_\infty \approx 266$ K, consistent with the value used in Fig. 2 and mentioned in the previous section. The location of the maximum temperature gradient is close to h_θ, and considerably higher than h_τ and h_J. The latter two heights are nearly equal, and lower than the SBL depth estimation based on TKE, perfectly in line with previous studies (Huang and Bou-Zeid 2013; Sullivan et al. 2016; Chinita et al. 2022).

Based on LES and field observations, semi-empirical formulas have been proposed to calculate the SBL depth from other flow characteristics (Zilitinkevich and Baklanov 2002; Zilitinkevich et al. 2007). In order to assess whether these also work for the equilibrium SBL with subsidence, we consider the following well-established expression in dimensional form (Zilitinkevich et al. 2007):

$$\frac{1}{h_{Zi}^2} = \left(\frac{f_c}{C_{TN}u_*}\right)^2 + \frac{f_c}{C_{NS}^2\kappa u_* L_O} + \frac{f_c N_\infty}{(C_{CN}u_*)^2} \tag{11}$$

with $\kappa = 0.4$ the Von Karman constant and $N_\infty = (\Gamma_\theta g/\theta_r)^{1/2}$ the Brunt-Väisälä frequency in the free atmosphere, where Γ_θ denotes the temperature gradient. For the empirical constants, we use $(C_{TN}, C_{NS}, C_{CN}) = (0.5, 0.78, 1.6)$ as determined by Liu et al. (2021a) and Narasimhan et al. (2023) from LES datasets. Equation (11) is essentially a squared reciprocal interpolation between the length scales that are relevant in a truly neutral boundary layer, SBL and CNBL, respectively (Zilitinkevich et al. 2007). Note that in the present simulations with subsidence, the CNBL contribution vanishes since $N_\infty = 0$. Estimates based on Eq. (11) are represented by the grey diamonds in Fig. 3, showing that the estimates are far off for the present SBLs with subsidence.

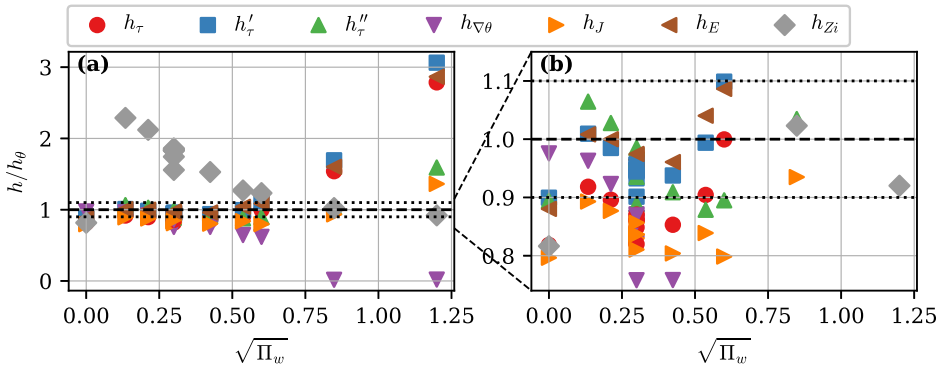

Fig. 3 Comparison of SBL depth estimations calculated through the methods 1-6 explained in the text, normalized with the thermal boundary-layer height h_θ. Grey diamonds refer to the estimated SBL depth h_{Zi} obtained through equation (11). Panel (b) is just a zoom of panel (a), while the black dotted lines indicate a 10% deviation between the h_θ and the other SBL height estimations

Zilitinkevich et al. (2002) proposed a correction to h_{Zi} derived from a relaxation equation of the actual SBL height to account for synoptic scale vertical motions: $h_{Zi-\mathrm{cor}} = h_{Zi} + w_h t_R$, with w_h the large-scale vertical velocity at the top of the SBL ($w_h = -\Gamma_w h$ in our case). For the relaxation timescale t_R, Zilitinkevich and Baklanov (2002) use $t_R = C_E/f_c$, while Zilitinkevich et al. (2007) recommend $t_R = C_E h/u_*$, with $C_E \approx 1$. Figure 3 however clearly shows that the error in h_{Zi} is not linear in Γ_w, implying that such a correction does not work here.

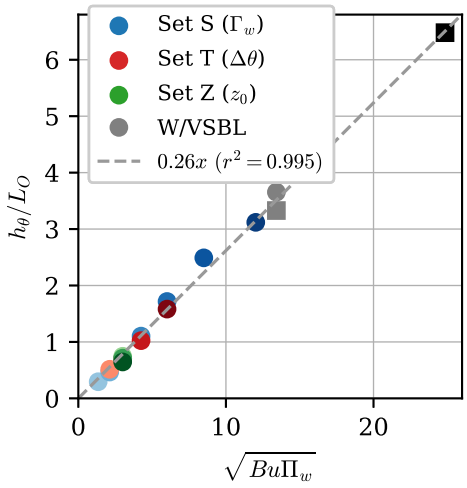

Fig. 4 Stability parameter h_θ/L_O compared against the square root of product of non-dimensional Buoyancy and Subsidence numbers. Each point represents one simulation: blue circles indicate simulations of set S with varying subsidence rate, red circles represent simulations of set T with varying temperature difference, and green circles are simulations of set Z with varying surface roughness. Darker colors imply higher values. The grey circle indicates WSBL-B24 case, while the grey and black squares represent data from the WSBL and VSBL cases of L19. The grey dashed line is the linear least-squares fit to the data: $y = 0.26x$ (cf. Eq. (12)) with coefficient of determination $r^2 = 0.995$

Based on our simulations, a different scaling for thermal boundary-layer height is proposed:

$$\frac{h_\theta}{L_O} = \frac{h_\theta \kappa g q_0}{\theta_r u_*^3} \approx C_h \sqrt{\Pi_w Bu}, \tag{12}$$

with L_O the Obukhov length, and Bu and Π_w the non-dimensional groups introduced before (Eq. 9). The ratio h/L_O is typically referred to as the stability parameter (e.g. Holtslag and Nieuwstadt

1986; Heisel and Chamecki 2023). $C_h \approx 0.26$ is determined through a least-squares fit with coefficient of determination $r^2 = 0.995$, as shown in Fig. 4. To assess the validity of Eq. (12) in a wider range of simulations, the WSBL and VSBL cases from L19 are also included in Fig. 4. Since h_θ is not reported, $h_\theta \approx 1.1 h_\tau$ is estimated based on our own WSBL simulation (see also Table 1 and Fig. 3). Of note, Eq. (12) does not depend on the third external parameter (z_0 or Ro_0), because including $\log(Ro_0)$ resulted in only negligible changes of r^2. In Sect. 3.4, the relation in Eq. (12) is used to estimate h_θ from external parameters only.

3.3 Scaling of Steady Mean Profiles

In order to assess similarity of mean variables, Fig. 5 presents scaled profiles of the simulations reported in Table 1. The horizontal velocity magnitude is scaled with the geostrophic wind G (Fig. 5a), temperature is normalized with the global temperature difference $\Delta\theta$ (Fig. 5c), while the vertical momentum- and heat fluxes are normalized with their respective surface values (Figs. 5b, d). The thermal boundary-layer height h_θ is used to normalize the vertical coordinate. Panel a) shows not only that the height where the LLJ occurs coincides in most cases (cf. Fig. 3), but also that the maximum wind speed is roughly equal ($\sim 1.1G$). The maximum wind speed is slightly lower for the cases with strongest subsidence (darker blue lines), while the LLJ is slightly stronger for the GABLS1 case ($\sim 1.2G$, dashed grey line). The scaled momentum flux profiles in Fig. 5b coincide remarkably well, even with the GABLS1 case.

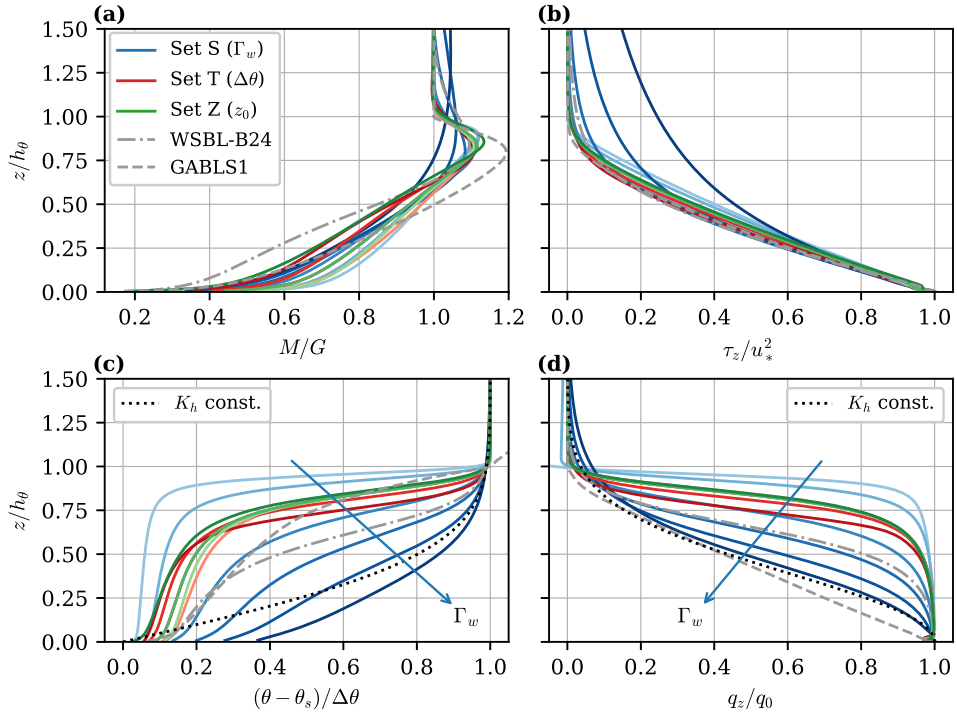

Fig. 5 Mean profiles of (a): horizontal wind magntiude scaled with geostrophic wind speed, (b) momentum flux normalized with surface momentum flux, (c) potential temperature scaled with global temperature difference and (d) heat flux scaled with surface heat flux. The vertical coordinate is scaled with thermal boundary-layer height h_θ. Line colors are the equal to Fig. 2: blue lines indicate varying subsidence rate (set S), red lines represent varying temperature difference (set T) and green lines denote varying surface roughness (set Z). The grey dashed and dash-dotted lines represent the GABLS1 and WSBL-B24 cases, respectively. In the bottom row, the black dotted lines are obtained analytically for constant eddy-diffusivity (see Eqs. (16)), while the blue arrows indicate direction of increasing subsidence rate

In line with the observations in the preceding section, only the the cases with strongest subsidence rate clearly deviate from the other profiles, i.e. the height where the shear stress vanishes is significantly higher than the depth of the thermal boundary layer. Since the temperature gradient above h_θ is negligible, this 'decoupling' of the thermal and turbulent boundary layer implies that a large portion of the turbulent motions is not damped by stratification. Figure 10e in Appendix 1 shows that in these cases, the gradient Richardson number in the thermal boundary layer does not reach the critical value of 0.25, which offers an explanation for the survival of turbulence and its penetration high into the domain (Sullivan et al. 2016, e.g.).

Figures 5c and d reveal that the shape of the normalized temperature and heat flux profiles is mainly determined by the subsidence rate Γ_w, as the blue curves clearly do not overlap. By contrast, the green and red curves, which indicate that the global temperature difference (or Bu) and surface roughness (or Ro_0) are varied, appear to be very similar. This finding is corroborated by L19, who remark that the temperature profiles in their WSBL and VSBL cases (where Π_w remains equal while both Bu and Ro_0 are changed, see Table 1) have the same overall shape. As discussed in the previous section, weak subsidence results in a nearly neutral boundary layer with strong capping inversion, whereas high subsidence rates result in a seemingly exponential (convex) temperature profile. The former 'convex-concave-convex' shape was also observed by L19, while the field observations, where they compared their simulations to, showed more convex or linear temperature profiles. They attributed this discrepancy to the lack of a radiation model or erroneous subsidence profile and magnitude. The present results demonstrate that a higher subsidence rate indeed leads to a more convex or linear temperature profile.

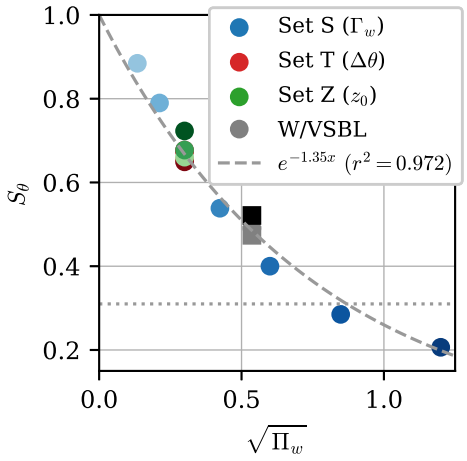

Fig. 6 Dependency of the shape factor of the temperature profile S_θ (Eq. (5)) on square-root of the non-dimensional subsidence rate Π_w. Colors and markers are equal to Fig. 4. The grey dashed line indicates the least-squares fit $y = \exp(-C_S x)$ with $C_S = 1.35$ and coefficient of determination $r^2 = 0.972$. Horizontal dotted line indicates the shape factor that would be obtained for constant eddy-diffusivity (see Eq. (16))

To quantify the shape of the temperature profile, the shape factor S_θ as defined in Eq. (5) is used. Figure 6 displays S_θ for all simulations as a function of $\Pi_w^{1/2}$. The good collapse of all cases from simulation sets T and Z (green and red markers) re-emphasizes that the scaled temperature profile is mainly determined by the dimensionless subsidence rate $\Pi_w = \Gamma_w / f_c$. For small subsidence rates, the shape factor approaches 1, as the scaled temperature profile has a rectangular shape with a thin inversion layer capping the near-neutral boundary layer (see Fig. 5c). For $\Pi_w \to 0$ and $S_\theta \to 1$, the temperature gradient in the inversion layer would go to infinity. Therefore, there should be a physical upper limit on S_θ and Π_w for which equilibrium is still possible, which it is expected to depend on a critical Richardson number in the inversion layer. Exploring this limit with LES however would require very fine grid resolutions in the strongly stratified inversion layer, which is beyond the scope of the present work (see also Appendix

1). On the other hand, increasing subsidence rate reduces the shape factor, which seems to go asymptotically towards 0 as shown by Fig. 6 (although it can be derived that in the limit of laminar flow, $S_\theta \approx 0.31$ (see below), as indicated by the horizontal dotted line).

To describe the dependency of S_θ on the subsidence rate, a linear regression to fit the exponential function is used,

$$S_\theta = \frac{q_0}{\Gamma_w h_\theta \Delta\theta} = \exp\left(-C_S(\Pi_w)^{1/2}\right) \tag{13}$$

to the data, resulting in $C_S = 1.35$. A least-squares fit of the curve $\exp(-C_S\Pi_w)$ (i.e. without the square root) resulted in a poor match with the data ($r^2 = 0.68$), motivating the choice for $\Pi_w^{1/2}$ on the horizontal axis of Fig. 6. The WSBL and VSBL cases from L19 (square markers) agree very well with the curve in Eq. 13, even though they have a significantly larger temperature difference (and Bu) and different geostrophic winds than the other simulations. This reinforces the conclusion that the temperature shape factor is predominantly controlled by subsidence rate.

Considering the normalized heat flux profiles in Fig. 5d, a similar statement can be made, i.e. the Buoyancy and Rossby number only have a small effect while subsidence rate mainly determines the shape of the profiles. This analogy is expected, since the equilibrium profiles of temperature and heat flux are directly related through the subsidence rate:

$$\frac{\partial\langle q_z\rangle}{\partial z} = \Gamma_w z \frac{\partial\langle\theta\rangle}{\partial z} \tag{14}$$

(see also Eq. (2)). The equation above explains for example why the vertical gradient of the turbulent heat flux approaches zero near the surface, as well as the correlation between the strong temperature gradient and large change in turbulent heat flux in the inversion layer.

By contrast, the GABLS1 case (grey dashed line in Fig. 5d), displays a linear heat flux profile. For such a quasi-stationary SBL without subsidence, Nieuwstadt (1984) already derived analytical expressions for the vertical fluxes of heat and momentum. For the heat flux, a linear profile $q_z/q_0 = (1 - z/h)$, was indeed obtained, in agreement with the LES results of the GABLS1 case. Assuming both the Richardson numbers based on fluxes and gradients to be equal to 0.2 throughout the boundary layer, Nieuwstadt (1984) derived $\tau_z/u_*^2 = (1 - z/h)^{3/2}$. Given that the GABLS1 profile in Fig. 5b approximately follows this equation (e.g. Beare et al. (2006)), and most of the profiles from present simulations have a similar shape; Nieuwstadt's momentum flux profile describes even the SBL with subsidence reasonably well in most cases. The fact that the heat flux profiles do not match is a consequence of the additional subsidence term in the temperature equation (see Eqs. (2) and (14)), which makes solving the system of equations from Nieuwstadt (1984, see his Appendix) less straightforward. Therefore, we did not succeed in deriving analytical flux profiles by adapting Nieuwstadt's derivation with an additional subsidence term.

A different approach to finding analytical expressions for the temperature and heat flux profiles, would be to assume a gradient diffusion hypothesis: $q_z = -K_h \partial\langle\theta/\rangle\partial z$, with K_h the (effective) eddy diffusivity. Substituting this in Eq. (14), leads to a linear differential equation for the potential temperature:

$$\frac{\partial}{\partial z}\left(-K_h \frac{\partial\langle\theta\rangle}{\partial z}\right) = \Gamma_w z \frac{\partial\langle\theta\rangle}{\partial z} \tag{15}$$

The most straightforward solution is obtained for constant K_h. With the appropriate boundary conditions, it can be shown that Eq. (15) then leads to the following normalized temperature and heat flux profiles:

$$\frac{\langle\theta\rangle - \theta_s}{\Delta\theta} = \mathrm{erf}\left(\frac{z}{\sqrt{2}\sigma_\theta}\right), \quad \frac{q_z}{q_0} = \exp\left(-\frac{z^2}{2{\sigma_\theta}^2}\right) \tag{16}$$

where erf is the error function and $\sigma_\theta = (K_h/\Gamma_w)^{1/2}$, a length scale composed of the effective eddy diffusivity and subsidence rate. We remark that this length scale resembles the more familiar Ekman depth scale $D_E = (2K_m/f_c)^{1/2}$, where the eddy diffusivity is replaced by the eddy viscosity, and the Coriolis frequency plays the role of subsidence rate. This scale can be derived directly from a momentum balance, see e.g. Zilitinkevich et al. (2002). Moreover, the turbulent eddy diffusivity K_h in Eq. 15 could be easily replaced by a (constant) molecular diffusivity for temperature, in which case the profiles in Eq. (16) can be interpreted as a result of laminar diffusion in the presence of subsidence, without any turbulent transport. Accordingly, σ_θ then

becomes analogous to the 'viscous Ekman layer depth' that is often used in DNS of Ekman layers (Coleman and Spalart 1990).

In order to obtain the expressions in Eq. (16) as a function of z/h_θ, we can use that $(\langle\theta\rangle - \theta_s)/\Delta\theta = 0.99$ at $z = h_\theta$ by definition, resulting in $\sigma_\theta/h_\theta = 0.388$. This allows to compare the non-dimensional temperature and heat flux profiles for constant K_h to the LES results, as shown by the black dotted lines in Figs. 5c and d. It is clear that the LES profiles do not match with these analytical solutions, which is due to the fact that the eddy diffusivity K_h is a function of z rather than constant. Remarkably, the heat flux profile in the case with the strongest subsidence (S7, darkest blue line) agrees rather well with the analytical profile. Inspection of the K_h-profiles (not shown) reveals that this is indeed the case where the eddy diffusivity shows the smallest variation with height. From the definition of the thermal shape factor (Eq. (5)) and the expressions in Eq. (16), it can be shown that $S_\theta = 0.31$ for the case of constant K_h, as indicated by the horizontal dotted line in figure 6. The fact that S_θ drops below this value for cases S6 and S7, suggests that there exists a local minimum for a certain value of Π_w, since the limit of Eq. (16) should be reached under extremely stable conditions where all turbulence is eliminated and the eddy diffusivity is replaced by the (constant) molecular thermal diffusivity.

The accuracy of the solution to Eq. (15) is expected to improve by including a height-dependent eddy diffusivity. Various parametrizations have been proposed for eddy viscosity (Brost and Wyngaard 1978; Nieuwstadt 1983), which could be adapted to the eddy diffusivity through $K_h \approx K_m/Pr_t$, with Pr_t the turbulent Prandtl number that may or may not be height dependent. Due to the large number of assumptions there, we did not find a general parametrization that described the actual $K_h(z)$ in the LESs accurately enough to produce solutions to Eq. (15) that matched the LES results satisfactory well. Hence, finding analytical solutions for equilibrium SBL profiles with subsidence, similar to Narasimhan et al. (2023) for the case without subsidence, remains a topic for future work.

3.4 A Simple Geostrophic Drag Law to Close the Model

From the empirical correlations (12) and (13) that were developed in the preceding section, the surface heat flux and thermal boundary-layer height can be predicted based on the external simulation parameters Π_w and Bu, if the friction velocity u_* is provided. A so-called geostrophic drag law (GDL) can be used to determine the geostrophic drag coefficient u_*/G (e.g. Zilitinkevich and Esau 2002)). A variety of GDLs has been proposed for different conditions, often in complicated formulations with dependencies on internal flow parameters such as boundary-layer height and geostrophic wind direction, and multiple empirical constants (Liu and Stevens 2021; Narasimhan et al. 2023, most recently). Instead, a formulation preferred is one where the dependent variables are fully determined by the relevant independent variables (given in Eq. (9)), following Swinbank (1974). For a neutral ABL and without taking wind direction into account, the basic relation $u_*/G = 0.111{Ro_0}^{-0.07}$ was found, valid in the range $10^4 < Ro_0 < 10^9$. Starting from this expression, the deviation between the simulations here and this neutral case are calculated. Realizing that this departure must be proportional to stability and subsidence effects, and thus eventually finding excellent agreement for the power-law form $G/u_* - (0.111{Ro_0}^{-0.07})^{-1} = C_g Bu^{p_1} \Pi_w^{p_2}$. The suitable values for p_1 and p_2 were determined through trial and error to be approximately 0.6 and 0.4, respectively. Figure 7 shows that a least squares fit with $C_g = 1.13$ works very well for the data in both the present study and L19.

The friction velocity u_* can then be predicted from solely external parameters via:

$$u_* = \frac{G}{C_r {Ro_0}^{0.07} + C_g Bu^{0.6} \Pi_w^{0.4}}. \tag{17}$$

with $C_r = 1/0.111 = 9$ and $C_g = 1.13$.

Together with Eqs. (12) and (13), Eq. (17) forms a closed model that can be used to estimate the friction velocity, surface heat flux and thermal boundary-layer height from external parameters in the present simulations of the SBL with subsidence. The model predictions are compared to the LES data in Fig. 8, where the top row shows correlations plots and the bottom row the relative error of the estimation. Every marker represents one LES case, where the squares indicate the WSBL and VSBL cases of L19. Maximal errors below 5% for q_0 and u_*, and around 10% for h_θ

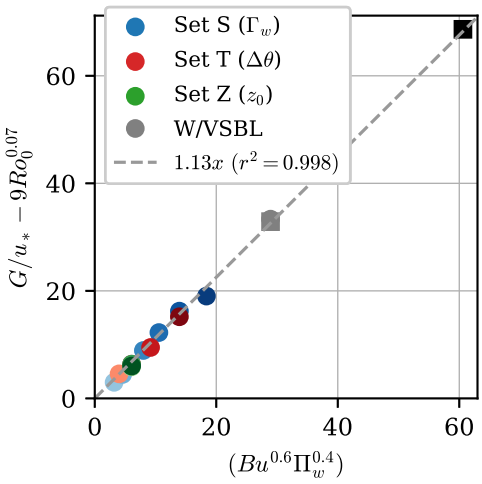

Fig. 7 Correlation between the reduced friction coefficient and product of non-dimensional Buoyancy and Subsidence numbers, leading to the geostrophic drag law in Eq. (17). See figure 4 for meaning of colors and markers. The grey dashed line indicates the least-squares linear fit $y = 1.13x$ with coefficient of determination $r^2 = 0.998$

are found. The match with the VSBL case from L19 (black squares in Fig. 8) suggests that the model also covers the very stable boundary layer regime, which exhibits intermittent turbulent bursts resulting from unstable internal waves (Van Der Linden et al. 2020).

3.5 Monin–Obukhov Similarity in the Presence of Subsidence

In this final section, we compare the results of the LESs of the equilibrium SBLs with subsidence to MOST (see Foken (2006) for a historical overview). Within this framework, the dimensionless gradients for momentum and heat play a central role:

$$\phi_m = \frac{\kappa z}{u_*}\left[\left(\frac{\partial u}{\partial z}\right)^2 + \left(\frac{\partial v}{\partial z}\right)^2\right]^{1/2}, \quad \text{and} \tag{18}$$

$$\phi_h = \frac{\kappa z}{\theta_*}\frac{\partial \theta}{\partial z}, \tag{19}$$

where $\theta_* = -q_0/u_*$ is the friction temperature. MOST assumes that these non-dimensional gradients are universal functions of the ratio z/L_O in the surface layer, and do not depend on other length scales such as surface roughness or ABL depth. Under weakly stable stratification ($0 < z/L_O \lesssim 1$), the consensus is that $\phi_{m,h}$ are linear functions of z/L_O (Heisel and Chamecki 2023, and references therein). Figures 9a and b show the dimensionless velocity and temperature gradients in the LESs with subsidence from the present study. Following Heisel and Chamecki (2023), data between $z = 0.03h_\theta$ and $0.3h_\theta$ is included, while the traditional limit of the surface layer is $z \approx 0.1h$. This height is illustrated by circular markers in Fig. 9. The widely used empirical similarity relations of the form $\alpha_{m/h} + \beta_{m/h}(z/L_O)$ from Businger et al. (1971) are indicated by the black dashed lines. It is clear that close to the surface (for $z < 0.1h_\theta$), the linear similarity relations hold reasonably well. One could argue that the match with MOST close to the surface is merely due to the fact that LES models used the flux-gradient relations from MOST to determine the surface fluxes, thereby enforcing this match. However, as discussed in Appendix 3, the heat flux due to subsidence at the first grid level is negligible compared to the surface heat flux, justifying the use of MOST as a boundary condition. For the dimensionless temperature gradient above $0.1h_\theta$, a departure from the linear profile depending on Buoyancy and subsidence numbers is observed. Remarkably, it seems that the simulations with stronger buoyancy and subsidence

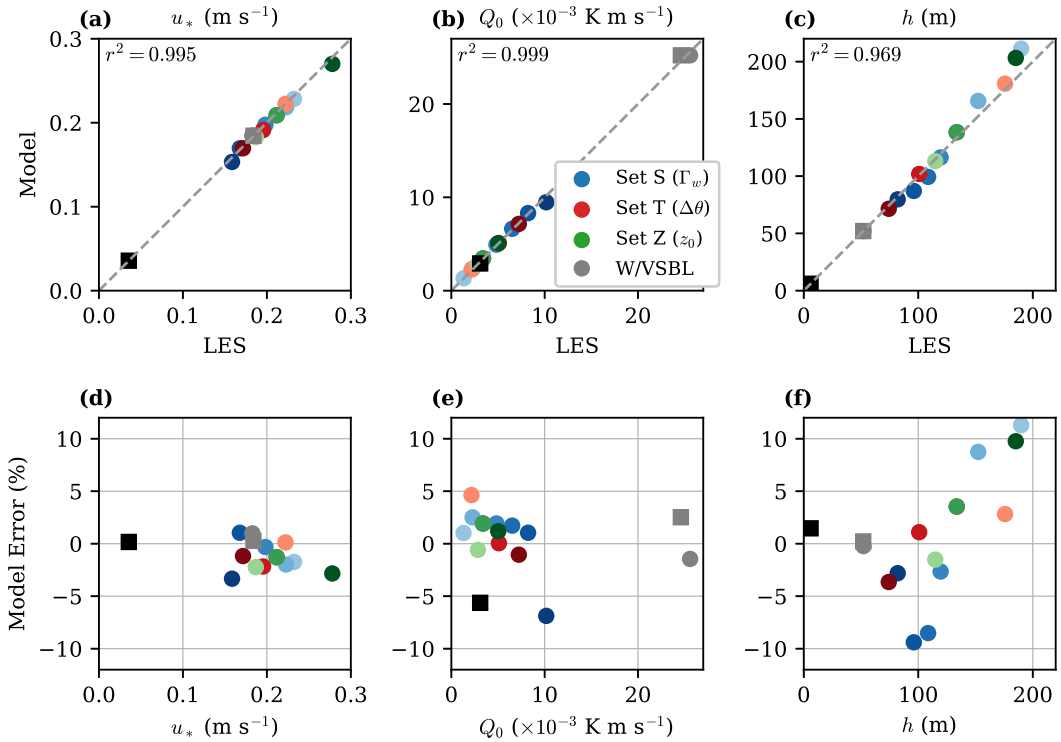

Fig. 8 (a-c): estimations of friction velocity, surface heat flux and thermal boundary-layer height through model equations (12), (13) and (17) compared against values from LES. (d-f): deviation of model predictions from LES value in percent. The meaning of colors and symbols is explained in the caption of Fig. 4. The grey dashed lines in the top row indicate $y = x$, while the r^2 values denote the coefficient of determination

effects are closer to the linear profile, as case S7 even (darkest blue line) exactly collapses on the relations from Businger et al. (1971).

In recent work by Heisel and Chamecki (2023), a new mixed scaling parameter for similarity in the SBL was introduced. Mixed scaling arguments have have been proposed successfully before, for instance the scaling of streamwise Reynolds stresses with a combination of the inner and outer velocity scales (Degraaff and Eaton 2000). In order to incorporate the effect of the boundary-layer depth h in MOST, Heisel and Chamecki (2023) propose to multiply the traditional scaling argument z/L_O by $(h/L_O)^{-1/2}$. It is shown that this new parameter $Z = z/(L_O h)^{1/2}$ provides improved similarity compared to the original MOST for high-resolution LES data from Sullivan et al. (2016) and field measurements from the CASES-99 campaign (Poulos et al. 2002), especially in the strongly stable regime. In an effort to corroborate their conclusions with an independent dataset, we compare the mixed scaling approach to data from the present steady SBLs with subsidence. In Sect. 3.2, h_θ/L_O is proportional to $(Bu\Pi_w)^{1/2}$ (see Eq. (12)), allowing the expression to be,

$$Z \approx Z' = \frac{z}{h_\theta} C_h^{1/2} (Bu\Pi_w)^{1/4} \tag{20}$$

thereby replacing one of the unknown internal parameters by external ones. Moreover, by cancelling L_O in the scaling argument Z, the problem of self-correlation due to common divisors u_*, θ_* in $\phi_{m/h}$ and z/L_O is effectively eliminated (as discussed by e.g. Klipp and Mahrt (2004); Baas et al. (2006); Sorbjan (2010); Heisel and Chamecki (2023)). Figures 9c and d show the dimensionless momentum and temperature gradients as function of Z', along with the linear relations (black dashed lines) proposed by Heisel and Chamecki (2023). The collapse is considerably improved for the ϕ_h profiles compared to the traditional MOST, although $\phi_h(Z')$ departs from the linear relation for $Z' > 0.2$. The enhancement in the similarity for the dimensionless momentum gradient in Fig. 9c is less evident. It seems that the ϕ_m profiles for simulation sets T and

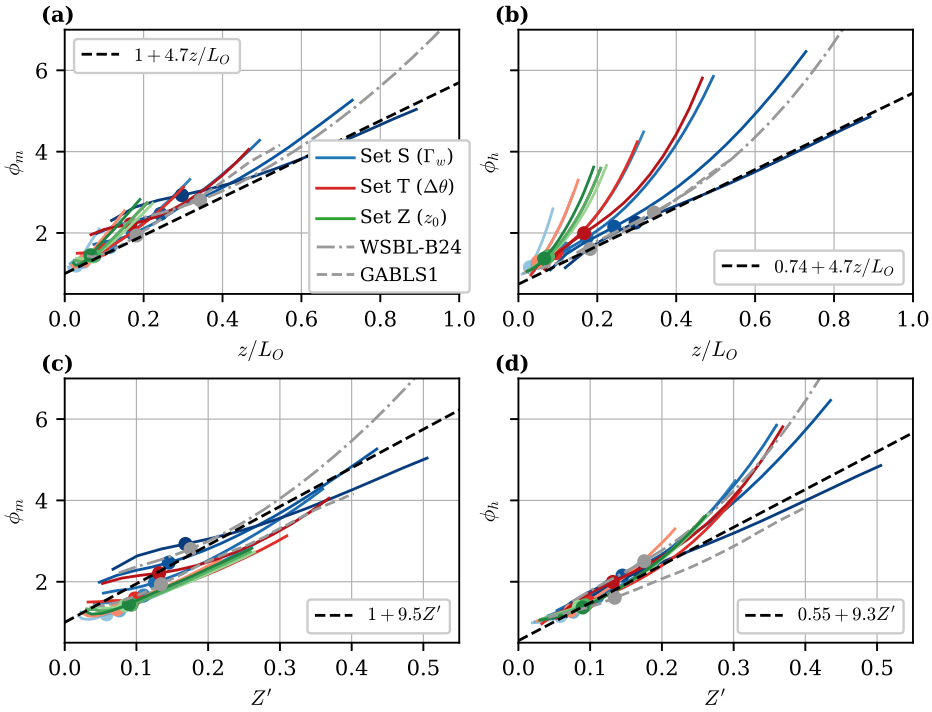

Fig. 9 Comparison of classic Monin–Obukhov similarity theory (a,b) and the mixed scaling similarity proposed by Heisel and Chamecki (2023) (c,d), by means of the dimensionless gradients for momentum (a,c) and temperature (b,d). The composite scaling parameter Z' is defined in Eq. 20. Only data in the range $0.03 < z/h_\theta < 0.3$ is included. The meaning of the colors corresponds to Fig. 5, and the linear black dashed lines correspond to empirical relations from (a,b) Businger et al. (1971) and (c,d) Heisel and Chamecki (2023)

Z match rather well, while the cases with strong subsidence from set S (dark blue lines) have a larger offset.

A last point to underline here is that Nieuwstadt (1984) introduced a 'local scaling' framework in order to extend MOST to the entire SBL. Plots similar to Fig. 9 with height-dependent values of the fluxes, and therefore a local Obukhov length, yield a substantially better collapse (not shown). For this local scaling system, the similarity relations from from Businger et al. (1971) with $\beta_{m/h} = 4.7$ overestimate the slope, while $\beta_{m/h} = 3$ as suggested previously by Chinita et al. (2022) fits better to the present LES data.

4 Conclusions

The statistically steady stably stratified ABL in the presence of subsidence has been investigated using a set of idealized large-eddy simulations, forced by a constant geostrophic wind $G = 8$ m s^{-1} and a linearly increasing subsidence velocity profile. By dimensional analysis, we show that the problem is governed by three non-dimensional groups: a surface Rossby number, a Buoyancy number and a dimensionless subsidence rate. To investigate the impact of these external parameters on the SBL, a range of different surface roughness lengths, subsidence rates and surface temperatures is considered. All simulations reached a truly steady state after 12 to 70 hours, where the cooling heat flux at the surface is compensated by the heating due to subsidence, resulting in thermal equilibrium. Hence, the present set of LES experiments extends previous research that showed subsidence can lead to a steady SBL (Mirocha and Kosović 2010; van der Linden et al. 2019) to a wider and less extreme range of conditions. Moreover, it allows to systematically investigate the impact of each governing parameter separately.

An examination of mean profiles reveals that all cases exhibit a low-level jet and constant temperature above some level. For increasing subsidence rate, the SBL changes from a near-neutral well-mixed layer capped by a strong inversion to a shallow, more stable ABL without capping inversion. Increasing the global temperature difference (i.e. decreasing the surface temperature) increases surface heat flux and reduces the height of the inversion layer, while a higher surface roughness results in a deeper SBL with more turbulence.

The thermal boundary-layer height is a consistent characterization of the SBL depth in thermal equilibrium, and is compared to previously used definitions of boundary-layer height in the SBL. Scaling the mean profiles with this length scale and the surface values results in an agreeable similarity of turbulent shear stress, except in cases with very strong subsidence, where the turbulence penetrates deep into the neutral free atmosphere. The normalized profiles of temperature and heat flux collapse for varying surface roughness or temperature, as their shape is mainly determined by the subsidence rate. Analytical expressions for these scaled mean profiles are derived for constant turbulent eddy-diffusivity K_h, but a more accurate parametrization of K_h would be required to describe the profiles of the present LES experiments.

From empirical correlations for the stability parameter h_θ/L_O, thermal shape factor S_θ and a new unidirectional geostrophic drag law, a model is formed that estimates relevant internal flow properties based on the three governing non-dimensional groups. For the present set of LES data, complemented by a weakly and very stable boundary layer case from van der Linden et al. (2019), the errors in predictions of surface heat flux and friction velocity are shown to be smaller than 5%, while the thermal boundary-layer height is estimated with a 10% accuracy.

A comparison of the dimensionless velocity and temperature gradients of the equilibrium profiles to MOST shows acceptable agreement in the surface layer. Higher up, similarity of non-dimensional temperature gradient is shown to be improved by using a new scaling argument that includes the thermal boundary-layer height and the non-dimensional Buoyancy and subsidence numbers, derived from the mixed scaling argument from Heisel and Chamecki (2023) and the empirical correlation of the stability parameter.

With the present investigation, light is shed on the complex relationship between subsidence, SBL depth, and surface fluxes, as well as the internal distribution of mean profiles of temperature, momentum and their vertical fluxes. Although a truly steady state may be encountered rarely in reality, the present stationary simulations could also be interpreted as an Eulerian view of a continuous transition from e.g. weak to strong subsidence or small to large vertical temperature difference, with each simulation representing a stage of the transition (Chung et al. 2012).

Finally, the steady-state SBL with subsidence could serve as a new benchmark case for LES. Moreover, the same principle of subsidence heating that compensates for surface cooling could be used in DNS of the SBL. The resulting stationary state allows for long averaging times and more formal comparison of multiple experiments (with different grid resolution, SGS models, wind-farm layout etc.) than a transient simulation with strong inertial oscillation such as the GABLS1 case (Sescu and Meneveau 2014; Maronga and Li 2022).

Acknowledgements The computational resources and services used in this work were provided by the VSC (Flemish Supercomputer Center), funded by the Research Foundation – Flanders (FWO) and the Flemish Government. The authors acknowledge financial support from the Research Foundation Flanders (T.B., FWO grant G098320N).

Data Availability Statement The processed data that supports the findings of this study will be made available upon acceptance of the manuscript.

Appendix 1: Resolution Sensitivity

To assess the sensitivity of our LES results to the grid resolution, we ran the three simulations with the strongest stability on a finer grid. These cases will be indicated as S6f, S7f and T4f. The grid size resolution is doubled with repsect to the cases in Table 1, i.e. $\Delta_x = \Delta_y = 1.56$ m in the horizontal directions and $\Delta_z = 0.78$ m vertically. For case T4f, the domain height was halved to $L_z = 200$ m in order to reduce computational cost. Given that both the momentum and heat flux profiles are constant above $h_\theta \approx 70$ m (see Fig. 2), it is safe to assume that

this does not affect the boundary layer itself. By contrast, the turbulence in cases S6 and S7 penetrates deeper into the free atmosphere (see Figs. 2 and 5), prohibiting to reduce the domain height. We note that these simulations were initialized from instantaneous flow fields of the cases with coarser grid, interpolated towards the finer mesh. Due to the pseudo-spectral discretization, horizontal interpolation was achieved through zero-padding the Fourier transform as explained in e.g. McWilliams et al. (2023). The fine-grid simulations were run for approximately 12 hours to allow the resolved small-scale turbulence to develop and reach a new thermal equilibrium state, after which the next 12.5 hours were used to collect statistics. Hence, the total runtime for each simulation was 24 physical hours.

Figure 10 shows the effect of increasing the grid resolution on the mean profiles of horizontal velocity (a), vertical momentum flux (b), potential temperature (c) and vertical heat flux (d). The differences between the fine and coarse grid cases appear rather limited, indicating that the grid-size used in this study is sufficient. The discrepancies are found to be largest for case T4f, which is also confirmed by comparing the global flow quantities in Table 2. We find that for cases S6 and S7 the impact of doubling the grid resolution on u_*, q_0 and h_θ is less than 1.5%, while in case T4f the surface heat flux and thermal boundary-layer height are reduced by approximately 2.5 and 9%, respectively. The reduction of boundary-layer height with increasing grid resolution is a known issue in LES, as discussed elaborately by Maronga and Li (2022). This is exemplified by the resolution sensitivity analysis by L19, which shows a 9% increase of SBL depth in their VSBL case when the grid spacing is raised by a factor 1.5. Following Sullivan et al. (2016), we also compare the gradient Richardson number Ri_g for the different grid resolutions in Fig. 10e. This height-dependent stability characteristic is defined as $Ri_g(z) = N^2/S^2$, where N is the Brunt-Vaisala frequency and $S = [(\partial u/\partial z)^2 + (\partial v/\partial z)^2]^{1/2}$ the mean shear. Both N^2 and S^2, and therefore Ri_g, are sensitive to mesh resolution. According to Sullivan et al. (2016), LES with (too) coarse resolution is unable to resolve small-scale vertical motions in the entrainment zone above the LLJ, because the Ozmidov Length becomes smaller than the grid spacing. As a result, S^2 decreases and Ri_g sharply increases above the critical value of 0.25. We indeed observe a strong peak in Ri_g around the top of the capping inversion ($z = h_\theta$) in case T4, while its magnitude is reduced in case T4f, related to reduced shear in the coarser-resolution case (not shown). For the two cases with high subsidence rate, S6 and S7, the critical Richardson number is not reached, allowing turbulence to penetrate higher into the atmosphere as mentioned in Sect. 3.

Matheou and Chung (2014) proposed a criterion for grid convergence based on the resolved TKE, stating that 90% of the TKE should be resolved for convergence of first-order statistics whereas 95% is required for second-order statistics. Fig. 10f displays the ratio between the SGS-TKE and the total TKE ($e_{tot} = (\tilde{u}_i\tilde{u}_i)/2 + e_{sgs}$). It is evident that the subgrid contribution reduces when a finer mesh is used. If we ignore the surface layer, the subgrid contribution is smaller than 20% in cases S6 and S7 and smaller than 15% in cases S6f and S7f. Hence, the requirement from Matheou and Chung (2014) is not met, yet given the small differences in Figs. a-d and Table 2, we still judge the grid resolution to be sufficient for the purpose of this study. Figure 10f further shows that in case T4, the SGS-TKE (and thus the subrid flux) goes to zero due to the strong stability in the inversion layer, while in simulation T4f the subrid TKE does not vanish. This is another indication that the inversion layer in case T4 is under-resolved. However, we remark that replacing the data from this coarse-resolution case by that from T4f does not alter any of the qualitative findings reported in the body of this paper. In fact, the normalized temperature and heat flux profiles from case T4f collapse better on the other profiles from set T in Figs. 5c and d (not shown).

Table 2 Global flow properties of the high-resolution simulations S6f, S7f and T4f. The relative error is defined as $\delta[\chi] = (\chi_f - \chi_c)/\chi_c$, where χ_f refers to the value from the simulations with the finer grid and χ_c to the coarser-grid simulation results given in Table 1.

Case	u_* (m s^{-1})	$\delta[u_*]$ (%)	q_0 (K m s^{-1})	$\delta[q_0]$ (%)	h_θ (m)	$\delta[h_\theta]$ (%)
S6f	0.169	0.41	-8.15×10^{-3}	-0.98	95.7	-0.41
S7f	0.161	1.38	-10.2×10^{-3}	0.00	80.9	-1.43
T4f	0.174	1.13	-7.05×10^{-3}	-2.47	67.6	-8.95

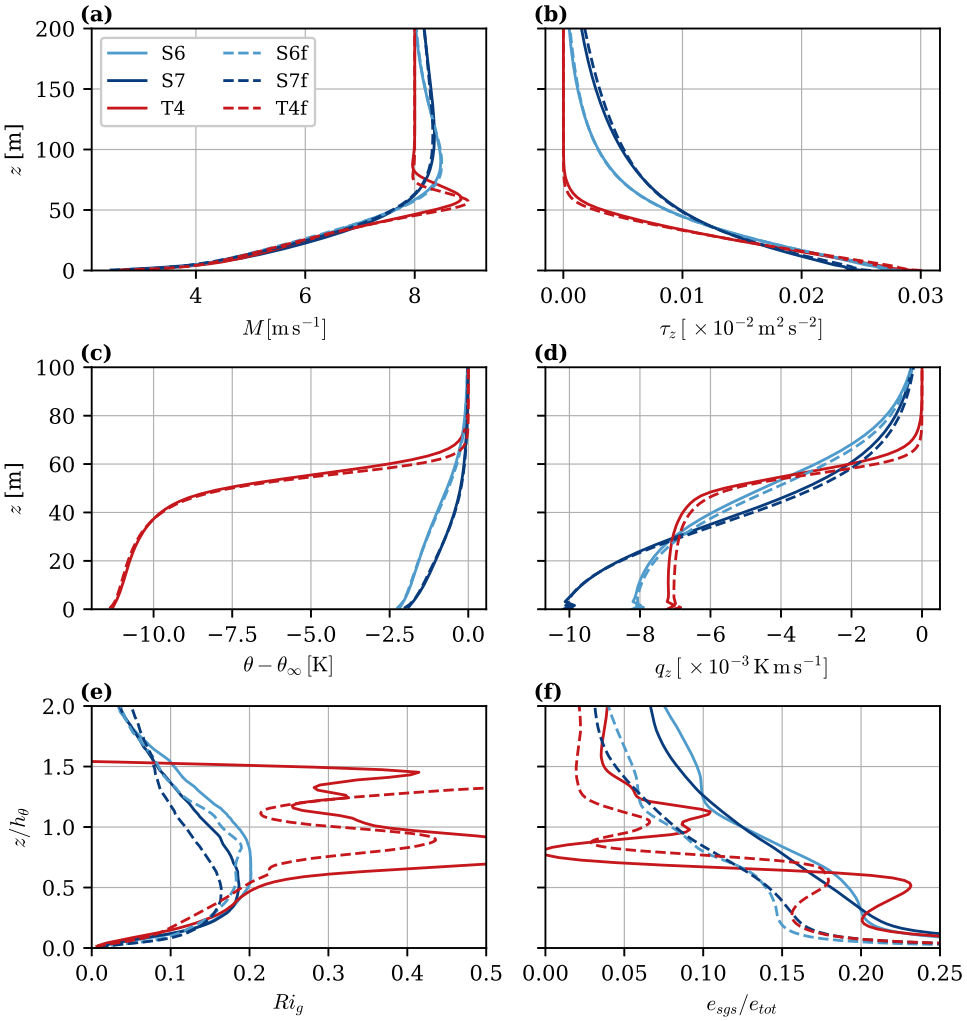

Fig. 10 Comparison of simulations S6, S7 and T4 (full lines) from Table 1 to simulations with doubled grid resolution (dashed lines). Subplots show mean wind speed (a), vertical momentum flux (b), potential temperature deviation (c), vertical heat flux (d), gradient Richardson number (e) and the ratio of subgrid to total TKE (f)

Appendix 2: Comparison to the Weakly Stable Boundary Layer Case from van der Linden et al. (2019)

Here, we compare the WSBL simulation from L19 to the results obtained with the present SP-Wind code. The full case setup is provided in tables 1 and 2 of L19, yet we shortly point out some key parameters and relevant differences between the WSBL-B24 and WSBL-L19 simulations. They mention they use a subsidence velocity of 4 mm s^{-1} at $z = 100$ m that was linearly interpolated to zero at the surface, corresponding to $\Gamma_w = \mathrm{d}w_s/\mathrm{d}z = 4 \times 10^{-5}\ \mathrm{s}^{-1}$. The geostrophic wind speed ($G = 12$ m s^{-1}), global temperature difference ($\Delta\theta = 25$ K), and reference temperature ($\theta_r = 235$ K) deviate from the the other simulations in the present study. The roughness length for momentum is $z_{0m} = 10^{-3}$ m, while the roughness length for temperature is one order of magnitude smaller. The domain size is $336 \times 336 \times 168$ m.

The main difference between the MicroHH code used by L19 and the SP-Wind code used here, is the discretization scheme. While they apply second-order finite differences for advection, SP-Wind is a pseudospectral code with Fourier-decomposition in the horizontal directions and a fourth-order finite difference scheme in the vertical direction. Motivated by this difference in discretization, case WSBL-B24 was computed with a grid spacing of $\Delta_x = \Delta_y = 1.31$ m and $\Delta_z = 0.7$ m, larger than the isotropic grid with $\Delta = 0.7$ m used by L19. Furthermore, L19 employ a Smagorinsky-Lily type eddy-viscosity model with a wall correction for the mixing length to calculate the subgrid fluxes, whereas the present simulations utilized a closure based on SGS-TKE (see Sect. 2.2).

The initialization procedure used in this study is outlined in Sect. 2.4.1. In case WSBL-B24 we used an initial temperature profile that increased linearly from θ_s to $\theta_s + 25$ K at $h_i = 50$ m, whereas L19 initialized their simulations with a constant temperature and cooled for 25 hours until the final surface temperature was reached. Subsequently, they continued the simulation for 5 hours and collected data from the final hour. In contrast, case WSBL-B24 was run for 32 physical hours in total, and the averaging window was a full inertial period (≈ 12.5 h) in which the heat flux due to subsidence was equal to the surface heat flux.

Figure 11 compares the mean profiles of horizontal velocity, flow angle and temperature for cases WSBL-L19 and WSBL-B24. An online data extractor tool was used to obtain the data from Fig. 5 in L19. These first-order profiles match rather well. For reference, the observational results from the Dome C site in Antarctica, where L19 compare their data to, is also included. The LES results agree well with these field measurements, except in the highest grid point as discussed by L19. The surface fluxes of the WSBL-L19 and WSBL-B24 are reported in Table 1, where the largest difference is a 4% deviation of the surface heat flux q_0. We further point out that the boundary-layer height calculated from the momentum flux profiles according to the first method in Sect. 3.2 is $h_\tau = 47.16$ m, equal to $h = 47.2$ m reported by L19. Overall, we conclude that the correspondence among the simulation results is good, especially considering the differences in numerical methodology outlined above.

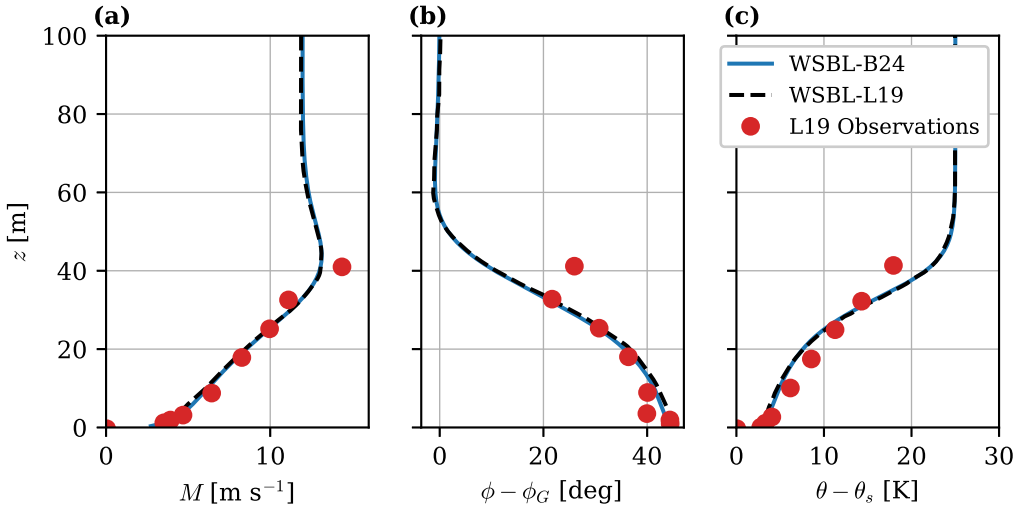

Fig. 11 Comparison of mean profiles of wind speed (a),relative wind direction (b) and potential temperature (c) for WSBL cases from the present study (blue lines) and L19 (black dashed lines). Data from from Fig. 5 in L19 was extracted using WebPlotDigitizer (apps.automeris.io/wpd/). Red circles indicate observed values from a measurement campaign in Antarctica as reported in L19

Appendix 3: A Short Note on Validity of Monin–Obukhov Similarity Theory as a Boundary Condition in Large-Eddy Simulations with subsidence

As there is a clear dependency of the dimensionless gradients $\phi_{m/h}$ on subsidence rate (see Fig. 9), the question arises whether the use of MOST for parametrization of surface fluxes is justified in the presence of subsidence. The simplest answer would be that the subsidence velocity approaches zero close to the surface, and is therefore negligible in the surface layer (e.g. Carlson and Stull 1985). We attempt to support this statement through a scaling argument, to illustrate that the heat flux due to subsidence is indeed negligible compared to the surface heat flux in the present simulation setup. Assuming MOST is valid and the dimensionless temperature gradient is linear in z/L_O, the (dimensional) temperature gradient is given by:

$$\frac{\partial \theta}{\partial z} = \frac{\theta_*}{\kappa z}\left(\alpha_h + \beta_h \frac{z}{L_O}\right). \tag{21}$$

Then the subsidence heating in the surface layer can be written as:

$$Q_{\text{subs}} = \Gamma_w z \frac{\partial \theta}{\partial z} = \frac{\Gamma_w \theta_*}{\kappa}\left(\alpha_h + \beta_h \frac{z}{L_O}\right). \tag{22}$$

Since MOST is only applied in the first layer of grid cells above the surface, we integrate (22) from z_0 up to the first grid level z_1 to find the effective subsidence heat flux in the first grid cell:

$$q_{\text{subs}} = \int_{z_0}^{z_1} Q_{\text{subs}} \mathrm{d}z = \frac{\Gamma_w \theta_*}{\kappa}\left(\alpha_h + \frac{\beta_h}{2}\frac{\Delta z_1}{L_O}\right)\Delta z_1, \tag{23}$$

where we assumed that $z_1 \gg z_0$ such that $z_1 - z_0$ can be replaced by the size of the first grid cell Δz_1. Furthermore, it should be safe to assumed that $\Delta z_1 \ll L_O$ and $\beta_h/2 \sim O(1)$, allowing the second term in Eq. (23) to be dropped. Then the ratio between the subsidence heat flux and the surface heat flux ($q_0 = -u_*\theta_*$) can be estimated as:

$$R_s = \frac{|q_{\text{subs}}|}{|q_0|} = \frac{\Gamma_w \Delta z_1}{\kappa u_*}. \tag{24}$$

To estimate this ratio in the simulations of the present study, we take $\Gamma_w \approx 10^{-4}$ s^{-1} , $\Delta z_1 \approx 1$ m and $u_* \approx 0.1$ m s^{-1}, resulting in $R_s \approx 2.5 \times 10^{-3} \ll 1$. With this, we prove that the heat flux due to subsidence in the first grid level is indeed negligible in comparison to the surface heat flux. Note that Eq. (24) in combination with the estimation of u_* given by Eq. (17) can be used to determine the grid spacing that is required to satisfy the condition that $R_q \ll 1$ a priori.

References

Allaerts D (2016) Large-eddy simulation of wind farms in conventionally neutral and stable atmospheric boundary layers. PhD thesis, KU Leuven

Allaerts D, Meyers J (2015) Large eddy simulation of a large wind-turbine array in a conventionally neutral atmospheric boundary layer. Physics of Fluids 27(6), DOI 10.1063/1.4922339

Allaerts D, Meyers J (2018) Gravity Waves and Wind-Farm Efficiency in Neutral and Stable Conditions. Boundary-Layer Meteorology 166(2):269–299, DOI 10.1007/s10546-017-0307-5

Ansorge C, Mellado JP (2014) Global Intermittency and Collapsing Turbulence in the Stratified Planetary Boundary Layer. Boundary-Layer Meteorology 153(1):89–116, DOI 10.1007/s10546-014-9941-3

Baas P, Steeneveld GJ, van de Wiel BJ, Holstlag AA (2006) Exploring self-correlation in flux-gradient relationships for stably stratified conditions. Journal of the Atmospheric Sciences 63(11):3045–3054, DOI 10.1175/JAS3778.1

Baas P, van de Wiel BJ, van Meijgaard E, Vignon E, Genthon C, van der Linden SJ, de Roode SR (2019) Transitions in the wintertime near-surface temperature inversion at Dome C, Antarctica. Quarterly Journal of the Royal Meteorological Society 145(720):930–946, DOI 10.1002/qj.3450

Beare RJ, Macvean MK, Holtslag AA, Cuxart J, Esau I, Golaz JC, Jimenez MA, Khairoutdinov M, Kosovic B, Lewellen D, Lund TS, Lundquist JK, McCabe A, Moene AF, Noh Y, Raasch S, Sullivan P (2006) An intercomparison of large-eddy simulations of the stable boundary layer. Boundary-Layer Meteorology 118(2):247–272, DOI 10.1007/s10546-004-2820-6

Bellon G, Stevens B (2012) Using the sensitivity of large-eddy simulations to evaluate atmospheric boundary layer models. Journal of the Atmospheric Sciences 69(5):1582–1601, DOI 10.1175/JAS-D-11-0160.1

Blackadar AK (1957) Boundary Layer Wind Maxima and Their Significance for the Growth of Nocturnal Inversions. Bulletin of the American Meteorological Society 38(5):283–290, DOI 10.1175/1520-0477-38.5.283

Blay-Carreras E, Pino D, Vilà-Guerau De Arellano J, Van De Boer A, De Coster O, Darbieu C, Hartogensis O, Lohou F, Lothon M, Pietersen H (2014) Role of the residual layer and large-scale subsidence on the development and evolution of the convective boundary layer. Atmospheric Chemistry and Physics 14(9):4515–4530, DOI 10.5194/acp-14-4515-2014

Bon T, Meyers J (2022) Stable Channel Flow with Spanwise Heterogeneous Surface Temperature. Journal of Fluid Mechanics pp 1–38, DOI 10.1017/jfm.2021.1113

Bon T, Broos D, Cal RB, Meyers J (2023) Secondary flows induced by two-dimensional surface temperature heterogeneity in stably stratified channel flow. Journal of Fluid Mechanics 970:1–36, DOI 10.1017/jfm.2023.619

Brost R, Wyngaard JC (1978) A model study of the Stably Stratified Planetary Boundary Layer. Journal of the Atmospheric Sciences 35:1427–1440

Businger JA, Wyngaard JC, Izumi Y, Bradley EF (1971) Flux-Profile Relationships in the Atmospheric Surface Layer. Journal of the Atmospheric Sciences 28:181–189

Carlson MA, Stull RB (1985) Subsidence in the Nocturnal Boundary Layer. Journal of Climate and Applied Meteorology

Castro IP, Kim JW, Stroh A, Lim HC (2021) Channel flow with large longitudinal ribs. Journal of Fluid Mechanics 915:1–28, DOI 10.1017/jfm.2021.110

Chinita MJ, Matheou G, Miranda PM (2022) Large-eddy simulation of very stable boundary layers. Part I: Modeling methodology. Quarterly Journal of the Royal Meteorological Society 148(745):1805–1823, DOI 10.1002/qj.4279

Chung D, Matheou G, Teixeira J (2012) Steady-state large-eddy simulations to study the stratocumulus to shallow cumulus cloud transition. Journal of the Atmospheric Sciences 69(11):3264–3276, DOI 10.1175/JAS-D-11-0256.1

Coleman GN, Spalart PR (1990) A numerical study of the turbulent Ekman layer. Journal of Fluid Mechanics 213:313–348, DOI 10.1017/S0022112090002348

Couvreux F, Bazile E, Rodier Q, Maronga B, Matheou G, Chinita MJ, Edwards J, van Stratum BJ, van Heerwaarden CC, Huang J, Moene AF, Cheng A, Fuka V, Basu S, Bou-Zeid E, Canut G, Vignon E (2020) Intercomparison of Large-Eddy Simulations of the Antarctic Boundary Layer for Very Stable Stratification, vol 176. Springer Netherlands, DOI 10.1007/s10546-020-00539-4

Csanady GT (1974) Equilibrium theory of the planetary boundary layer with an inversion lid. Boundary-Layer Meteorology 6(1-2):63–79, DOI 10.1007/BF00232477

Dai Y, Basu S, Maronga B, de Roode SR (2021) Addressing the Grid-Size Sensitivity Issue in Large-Eddy Simulations of Stable Boundary Layers. Boundary-Layer Meteorology 178(1):63–89, DOI 10.1007/s10546-020-00558-1

Degraaff DB, Eaton JK (2000) Reynolds-number scaling of the flat-plate turbulent boundary layer. Journal of Fluid Mechanics 422:319–346, DOI 10.1017/S0022112000001713

Devenport WJ, Lowe KT (2022) Equilibrium and non-equilibrium turbulent boundary layers. Progress in Aerospace Sciences 131(August 2021):100,807, DOI 10.1016/j.paerosci.2022.100807

Flores O, Riley JJ (2011) Analysis of Turbulence Collapse in the Stably Stratified Surface Layer Using Direct Numerical Simulation. Boundary-Layer Meteorology 139(2):241–259, DOI 10.1007/s10546-011-9588-2

Foken T (2006) 50 years of the Monin-Obukhov similarity theory. Boundary-Layer Meteorology 119(3):431–447, DOI 10.1007/s10546-006-9048-6

Gibbs JA, Fedorovich E (2016) Sensitivity of turbulence statistics in the lower portion of a numerically simulated stable boundary layer to parameters of the Deardorff subgrid turbulence model. Quarterly Journal of the Royal Meteorological Society 142(698):2205–2213, DOI 10.1002/qj.2818

Gohari SM, Sarkar S (2017) Direct Numerical Simulation of Turbulence Collapse and Rebirth in Stably Stratified Ekman Flow. Boundary-Layer Meteorology 162(3):401–426, DOI 10.1007/s10546-016-0206-1

Gohari SM, Sarkar S (2018) Stratified Ekman layers evolving under a finite-time stabilizing buoyancy flux. Journal of Fluid Mechanics 840:266–290, DOI 10.1017/jfm.2018.58

Goit JP, Meyers J (2015) Effect of ekman layer onwindfarm roughness and displacement height. ERCOFTAC Series 20(January):423–434

Heisel M, Chamecki M (2023) Evidence of Mixed Scaling for Mean Profile Similarity in the Stable Atmospheric Surface Layer. Journal of the Atmospheric Sciences 80(8):2057–2073, DOI 10.1175/JAS-D-22-0260.1

Holton JR (2004) An introduction to dynamic meteorology, 4th edn. Elsevier Academic Press, Amsterdam

Holtslag AA, Nieuwstadt FT (1986) Scaling the atmospheric boundary layer. Boundary-Layer Meteorology 36(1-2):201–209, DOI 10.1007/BF00117468

Huang J, Bou-Zeid E (2013) Turbulence and vertical fluxes in the stable atmospheric boundary layer. Part I: A large-eddy simulation study. Journal of the Atmospheric Sciences 70(6):1513–1527, DOI 10.1175/JAS-D-12-0167.1

Klemp J, Lily D (1977) Numerical Simulation of Hydrostatic Mountain Waves. Journal of atmospheric sciences 35:78–107

Klipp CL, Mahrt L (2004) Flux-gradient relationship, self-correlation and intermittency in the stable boundary layer. Quarterly Journal of the Royal Meteorological Society 130(601 PART B):2087–2103, DOI 10.1256/qj.03.161

Lanzilao L, Meyers J (2022) An Improved Fringe-Region Technique for the Representation of Gravity Waves in Large Eddy Simulation with Application to Wind Farms. Boundary-Layer Meteorology DOI 10.1007/s10546-022-00772-z

Lanzilao L, Meyers J (2024) A parametric large-eddy simulation study of wind-farm blockage and gravity waves in conventionally neutral boundary layers. Journal of Fluid Mechanics 979, DOI https://doi.org/10.1017/jfm.2023.1088

van der Linden SJ, Edwards JM, van Heerwaarden CC, Vignon E, Genthon C, Petenko I, Baas P, Jonker HJ, van de Wiel BJ (2019) Large-Eddy Simulations of the Steady Wintertime Antarctic Boundary Layer. Boundary-Layer Meteorology 173(2):165–192, DOI 10.1007/s10546-019-00461-4

Liu L, Stevens RJ (2021) Effects of atmospheric stability on the performance of a wind turbine located behind a three-dimensional hill. Renewable Energy 175:926–935, DOI 10.1016/j.renene.2021.05.035

Liu L, Gadde SN, Stevens RJ (2021a) Geostrophic drag law for conventionally neutral atmospheric boundary layers revisited. Quarterly Journal of the Royal Meteorological Society 147(735):847–857, DOI 10.1002/qj.3949

Liu L, Gadde SN, Stevens RJ (2021b) Universal Wind Profile for Conventionally Neutral Atmospheric Boundary Layers. Physical Review Letters 126(10):104,502, DOI 10.1103/PhysRevLett.126.104502

Lloyd CJ, Dorrell RM, Caulfield CP (2022) The coupled dynamics of internal waves and hairpin vortices in stratified plane Poiseuille flow. Journal of Fluid Mechanics 934:1–39, DOI 10.1017/jfm.2021.1007

Maas O, Raasch S (2022) Wake properties and power output of very large wind farms for different meteorological conditions and turbine spacings: a large-eddy simulation case study for the German Bight. Wind Energy Science 7(2):715–739, DOI 10.5194/wes-7-715-2022

Mahrt L (1999) Stratified atmospheric boundary layers. Boundary-Layer Meteorology 90(3):375–396, DOI 10.1023/A:1001765727956

Maronga B, Li D (2022) An Investigation of the Grid Sensitivity in Large-Eddy Simulations of the Stable Boundary Layer. Boundary-Layer Meteorology 182(2):251–273, DOI 10.1007/s10546-021-00656-8

Maronga B, Knigge C, Raasch S (2020) An Improved Surface Boundary Condition for Large-Eddy Simulations Based on Monin–Obukhov Similarity Theory: Evaluation and Consequences for Grid Convergence in Neutral and Stable Conditions. Boundary-Layer Meteorology 174(2):297–325, DOI 10.1007/s10546-019-00485-w

Matheou G, Chung D (2014) Large-eddy simulation of stratified turbulence. Part II: Application of the stretched-vortex model to the atmospheric boundary layer. Journal of the Atmospheric Sciences 71(12):4439–4460, DOI 10.1175/JAS-D-13-0306.1

Mazzitelli IM, Cassol M, Miglietta MM, Rizza U, Sempreviva AM, Lanotte AS (2014) The role of subsidence in a weakly unstable marine boundary layer: A case study. Nonlinear Processes in Geophysics 21(2):489–501, DOI 10.5194/npg-21-489-2014

McWilliams JC, Meneveau C, Patton EG, Sullivan PP (2023) Stable Boundary Layers and Subfilter-Scale Motions. Atmosphere 14(7):1–26, DOI 10.3390/atmos14071107

Mirocha JD, Kosović B (2010) A large-eddy simulation study of the influence of subsidence on the stably stratified atmospheric boundary layer. Boundary-Layer Meteorology 134(1):1–21, DOI 10.1007/s10546-009-9449-4

Mirocha JD, Kosović B, Curry JA (2005) Vertical heat transfer in the lower atmosphere over the Arctic Ocean during clear-sky periods. Boundary-Layer Meteorology 117(1):37–71, DOI 10.1007/s10546-004-1130-3

Mironov DV, Sullivan PP (2016) Second-moment budgets and mixing intensity in the stably stratified atmospheric boundary layer over thermally heterogeneous surfaces. Journal of the Atmospheric Sciences 73(1):449–464, DOI 10.1175/JAS-D-15-0075.1

Narasimhan G, Gayme DF, Meneveau C (2023) Analytical model coupling Ekman and surface layer structure in atmospheric boundary layer flows. Boundary-Layer Meteorology 123, DOI 10.1007/s10546-024-00859-9

Nieuwstadt F (1983) On the solution of the stationary, baroclinic ekman-layer equations with a finite boundary-layer height. Boundary-Layer Meteorology 26(4):377–390

Nieuwstadt F (1984) The Turbulent Structure of the Stable, Nocturnal Boundary Layer. Journal of the Atmospheric Sciences 41(14):2202

Nieuwstadt FT (2005) Direct numerical simulation of stable channel flow at large stability. Boundary-Layer Meteorology 116(2):277–299, DOI 10.1007/s10546-004-2818-0

Poulos GS, Blumen W, Fritts DC, Lundquist JK, Sun J, Burns SP, Nappo C, Banta R, Newsom R, Cuxart J, Terradellas E, Balsley B, Jensen M (2002) CASES-99: A comprehensive investigation of the stable nocturnal boundary layer. Bulletin of the American Meteorological Society 83(4):555–581, DOI 10.1175/1520-0477(2002)083⟨0555:CACIOT⟩2.3.CO;2

Rey-Sanchez C, Wharton S, Vilà-Guerau de Arellano J, Paw U KT, Hemes KS, Fuentes JD, Osuna J, Szutu D, Ribeiro JV, Verfaillie J, Baldocchi D (2021) Evaluation of Atmospheric Boundary Layer Height From Wind Profiling Radar and Slab Models and Its Responses to Seasonality of Land Cover, Subsidence, and Advection. Journal of Geophysical Research: Atmospheres 126(7):1–32, DOI 10.1029/2020JD033775

Saiki EM, Moeng CH, Sullivan PP (2000) Large-eddy simulation of the stably stratified planetary boundary layer. Boundary-Layer Meteorology 95(1):1–30, DOI 10.1023/A:1002428223156

Schäfer K, Frohnapfel B, Mellado JP (2022) The effect of spanwise heterogeneous roughness on mixed convection in turbulent channels. Journal of Fluid Mechanics pp 1–34, DOI 10.1017/jfm.2022.773

Sescu A, Meneveau C (2014) A control algorithm for statistically stationary large-eddy simulations of thermally stratified boundary layers. Quarterly Journal of the Royal Meteorological Society 140(683):2017–2022, DOI 10.1002/qj.2266

Shah SK, Bou-Zeid E (2014) Direct numerical simulations of turbulent Ekman layers with increasing static stability: Modifications to the bulk structure and second-order statistics. Journal of Fluid Mechanics 760:494–539, DOI 10.1017/jfm.2014.597

Shi Y, Zeng Q, Liu L, Huo J, Zhang Z, Ding W, Hu F (2022) Observed Evidence That Subsidence Process Stabilizes the Boundary Layer and Increases the Ground Concentration of Secondary Pollutants. Journal of Geophysical Research: Atmospheres 127(19):1–19, DOI 10.1029/2021JD035244

Sorbjan Z (2010) Gradient-based scales and similarity laws in the stable boundary layer. Quarterly Journal of the Royal Meteorological Society 136(650):1243–1254, DOI 10.1002/qj.638

Steeneveld GJ (2014) Current challenges in understanding and forecasting stable boundary layers over land and ice. Frontiers in Environmental Science 2(OCT):1–6, DOI 10.3389/fenvs.2014.00041

Stipa S, Ajay A, Allaerts D, Brinkerhoff J (2023) TOSCA - An Open-Source Finite-Volume LES Environment for Wind Farm Flows. Wind Energy Science Discussions pp 1–41

Stoll R, Porté-Agel F (2009) Surface heterogeneity effects on regional-scale fluxes in stable boundary layers: Surface temperature transitions. Journal of the Atmospheric Sciences 66(2):412–431, DOI 10.1175/2008JAS2668.1

Stoll R, Gibbs JA, Salesky ST, Anderson W, Calaf M (2020) Large-Eddy Simulation of the Atmospheric Boundary Layer. Boundary-Layer Meteorology 177(2-3):541–581, DOI 10.1007/s10546-020-00556-3

Strickland JM, Gadde SN, Stevens RJ (2022) Wind farm blockage in a stable atmospheric boundary layer. Renewable Energy 197(July):50–58, DOI 10.1016/j.renene.2022.07.108

Stull RB (1988) An introduction to boundary layer meteorology. Kluwer

Sullivan PP, Weil JC, Patton EG, Jonker HJ, Mironov DV (2016) Turbulent winds and temperature fronts in large-eddy simulations of the stable atmospheric boundary layer. Journal of the Atmospheric Sciences 73(4):1815–1840, DOI 10.1175/JAS-D-15-0339.1

Swinbank WC (1974) The geostrophic drag coefficient. Boundary-Layer Meteorology 7(1):125–127, DOI 10.1007/BF00224976

Tennekes H (1973) The Logarithmic Wind Profile. Journal of the 30:234–238

Van Der Linden SJ, Van De Wiel BJ, Petenko I, Van Heerwaarden CC, Baas P, Jonker HJ (2020) A businger mechanism for intermittent bursting in the stable boundary layer. Journal of the Atmospheric Sciences 77(10):3343–3360, DOI 10.1175/JAS-D-19-0309.1

Van Heerwaarden CC, Van Stratum BJ, Heus T, Gibbs JA, Fedorovich E, Mellado JP (2017) MicroHH 1.0: A computational fluid dynamics code for direct numerical simulation and large-eddy simulation of atmospheric boundary layer flows. Geoscientific Model Development 10(8):3145–3165, DOI 10.5194/gmd-10-3145-2017

Verstappen RW, Veldman AE (2003) Symmetry-preserving discretization of turbulent flow. Journal of Computational Physics 187(1):343–368, DOI 10.1016/S0021-9991(03)00126-8

Vignon E, Genthon C, Barral H, Amory C, Picard G, Gallée H, Casasanta G, Argentini S (2017a) Momentum- and Heat-Flux Parametrization at Dome C, Antarctica: A Sensitivity Study. Boundary-Layer Meteorology 162(2):341–367, DOI 10.1007/s10546-016-0192-3

Vignon E, Hourdin F, Genthon C, Gallée H, Bazile E, Lefebvre MP, Madeleine JB, van de Wiel BJ (2017b) Antarctic boundary layer parametrization in a general circulation model: 1-D simulations facing summer observations at Dome C. Journal of Geophysical Research 122(13):6818–6843, DOI 10.1002/2017JD026802

Wang X, Castillo L (2003) Asymptotic solutions in forced convection turbulent boundary layers. Journal of Turbulence 4(March 2003), DOI 10.1088/1468-5248/4/1/006

van de Wiel BJ, Moene AF, Steeneveld GJ, Baas P, Bosveld FC, Holtslag AA (2010) A conceptual view on inertial oscillations and nocturnal low-level jets. Journal of the Atmospheric Sciences 67(8):2679–2689, DOI 10.1175/2010JAS3289.1

Wyngaard JC (2010) Turbulence in the Atmosphere. Cambridge University Press, New York

Zilitinkevich S, Baklanov A (2002) Calculation of the height of the stable boundary layer in practical applications. Boundary-Layer Meteorology 105(3):389–409, DOI 10.1023/A:1020376832738

Zilitinkevich S, Baklanov A, Rost J, sofi Smedman A, Lykosov V, Calanca P (2002) Diagnostic and prognostic equations for the depth of the stably strafied Ekman boundary layer. Quarterly Journal of the Royal Meteorological Society 128(579):25–46, DOI 10.1256/00359000260498770

Zilitinkevich S, Esau I, Baklanov A (2007) Further comments on the equilibrium height of neutral and stable planetary boundary layers. Quarterly Journal of the Royal Meteorological Society 133(622):265–271, DOI 10.1002/qj.27

Zilitinkevich SS, Esau IN (2002) On integral measures of the neutral barotropic planetary boundary layer. Boundary-Layer Meteorology 104(3):371–379, DOI 10.1023/A:1016540808958